Department of Electrical Engineering and Automation

Mechanical study and optimization of a multi material rotor in a high speed synchronous reluctance machine

Thiriet Martin

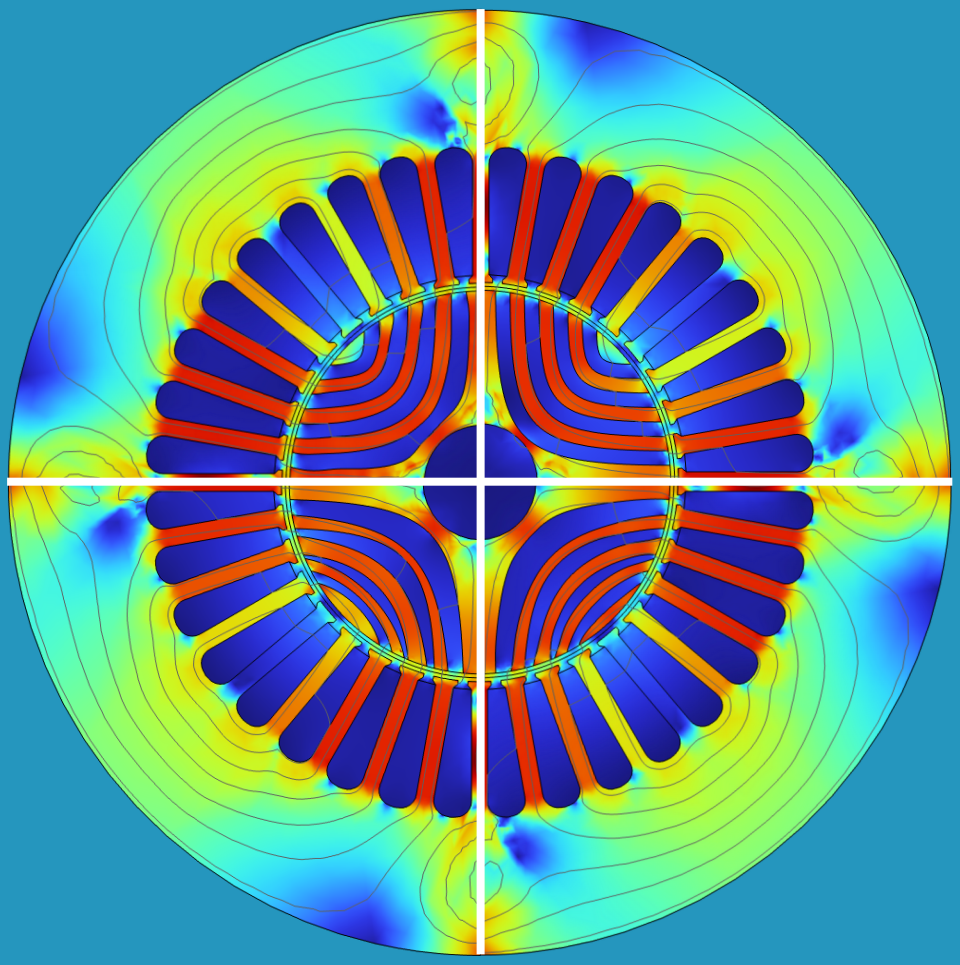

Supervised by: M. Poncelet, M. Sitnikov, J. Taurines, A. Belachen

Aalto University
School of Electrical
Engineering

école
normale
supérieure
paris—saclay

Contents

List of symbols and Abbreviations

Operators

atan2 arc tangent 2 function

$\overline{.}$ average operator over time

$[a, b]$ closed interval between a and b in $\mathbb{R}$

$[\![a, b]\!]$ closed interval between a and b in $\mathbb{N}$

$\circ$ composition of functions

$\cdot$ dot product

: double dot product

div divergence function

Δ delta operator

! factorial function

inf inferior bond for a domain with respect to the norm $||.||_\infty$

$||.||_\infty$ infinite norm

$\mathbb{I}$ identity matrix

min, max minimum and maximum function

∇ nabla operator

$\vdash$ quotient euclidean division

$\mathbb{R}$ set of real numbers

$\mathbb{N}$ set of integer

$^t.$ transpose operator

Greek symbols

α coefficient of the bezier optimizer

β scaling factor for the cost function

Γ angle

γ friction coefficient between the rotor and the shaft

δ interference between the rotor and shaft

$\boldsymbol{\epsilon}$ strain tensor

ϵ_{ij} component ij of $\boldsymbol{\epsilon}$

$\eta_{\%}$ efficiency

Θ angle of the bond

θ load angle of the motor

θ_e angle of the magnetic field field

θ_m angle of the rotor

κ coefficient of the bezier optimizer

λ lame material coefficient

μ lame material coefficient

μ_0 vacuum permeability

ν poisson ratio

ρ density, ρ_I density of Inconel, ρ_s density of silicon steel

$\boldsymbol{\sigma}$ stress tensor

σ_{ij} component ij of $\boldsymbol{\sigma}$

σ_τ shear component of $\boldsymbol{\sigma}$

τ local variable in $\mathbb{R}$

ϕ magnetic flux

$\cos\phi$ power factor

ω rotational speed of the motor

ω_e rotational speed of the magnetic field

Latin symbols

A magnetic vector potential field

B magnetic field

$\mathbb{C}$ stiffness tensor

$\tilde{\mathbb{C}}$ homogenized stiffness tensor

C cost function used for the optimization

c concentration, with c_I and c_s the concentration of Inconel and silicon steel respectively

D the diffusion coefficient and D_0 initial diffusion coefficient

E electric field

E Young modulus

E_a energy activation

f volume fraction with f_I the volume fraction of Inconel and f_s for the silicon steel

I current

$\mathbf{J}$ current density field

L length higher the the diffusion length

L_i Inductance

L_d^i,L_q^i Inductance in the dq frame

l length of the shaft

l_v, l_i minimum length and variation in the air gap length

M_{odel} theoretical model to optimize

m index in $\mathbb{N}$

m_i middle point defining the Bézier curve

N_p number of poles

N_σ norm of $\boldsymbol{\sigma}$

n normal vector

n number of rib

n_{rib} maximum number of rib

P pressure between the rotor and the shaft

P_{los} power losses

R universal gas constant

R_{ipple} ripple calculated with the min max function

R_{ipple}^{∞} ripple calculated with the approximation of the min max function

R_{ipple}^{+} positive part of the ripple with reference to the average

R_{ipple}^{-} negative part of the ripple with reference to the average

r radius

r_{rotor} rotor radius

r_{shaft} diameter of the shaft

$\mathbb{S}^E$ the Eshlby tensor

S surface of the air gap

Sx_{ini}, Sm_{ini}, Sw_{ini} initial gaps for the rib parameters

Sx_{lid}, Sm_{mid}, Sw_{mid} gap between consecutive rib parameters

Sx_{end}, Sm_{end}, Sw_{end} final gaps for the rib parameters

$T(t)$ torque for a time simulation

$T(\theta)$ torque for a sweep simulation

T_{ripple} torque ripple

T° temperature

$\overline{T}$ time average of the torque

T_{ipple} torque ripple by default calculated with min max criteria

t time in time simulation

u displacement vector

u_i component of the displacement

V volume

V_d,V_q voltage in the dq frame

v vector of parameters

w_i weight point defining the Bézier curve

x_i first points defining the Bézier curve

Abbreviations

ALA Axially laminated rotor

SynRm Synchronous reluctance motor

The escalating energy costs in recent years have compelled manufacturers to adopt more efficient devices. This pursuit of enhanced efficiency is universal across various sectors, spanning from internal combustion engines to electric motors. Achieving even small improvements in performance levels in electric motors can yield substantial energy saving globally. Electric motors account for approximately 40% to 45% of the overall global electricity consumption. Hence, even marginal improvements could translate into noteworthy energy conservation, concurrently aiding in the reduction of environmental pollutants.

This inclination towards augmenting the performance of electric motors is notably pronounced in the realm of high-speed, high-power motors. Such motors necessitate an intricate comprehension of the underlying physics that enables them to operate and sustain elevated speeds. Theses motors are on the edge of what is possible with current material technology and pushing its limits. Nonetheless, the development of such motors in needed to fulfill the need for high power, high speed electric motor.

1 Introduction to high speed synchronous reluctance motors

1.1 Applications high speed motors

High-speed motors find utility across a spectrum of demanding scenari. In contemporary times, one prominent application domain for high-speed motors is within electric vehicles, as evidenced by A. Credo's work in [1]. In this context, motor speeds range from 10000 rpm to 16000 rpm. However, the gamut of applications extends much further, as demonstrated by C. Zwyssig [2]. High-speed motors find extensive utilization in diverse industrial spheres such as flywheels, gas turbines, and gas compressors, where speeds can soar to 40000 rpm, and motor power can scale into tens of kilowatts. This underscores the escalating demand for high-speed, high-efficiency motors.

While various motor types can attain elevated speeds, certain categories exhibit inherent limitations.

The high-speed induction motor, investigated by G. Buticchi [3], represents one avenue towards achieving elevated rotational speeds. Notably economical due to material choices, but these high-speed motors lag in power density and overall efficiency. This reduced efficiency arises from the imperative for the rotor to induce eddy currents, thereby relying on inherent losses. Consequently, these motors are not often the preferred choice for high-speed applications.

Contrastingly, the high-speed permanent magnet motor, explored by Z. Zhang [4], stands out as a widely favored option for high-speed and high-efficiency endeavors. These motors can achieve remarkable efficiency and commendable power density. However, their construction relies heavily on the utilization of permanent magnets crafted from rare earth materials. The scarcity, elevated cost, and susceptibility to demagnetization following prolonged usage reduces the usage of this type of motors.

Another promising avenue lies in the adoption of synchronous reluctance motors. Crafted from cost-effective materials, they exhibit immunity to demagnetization and the potential for high efficiency. Consequently, these motors hold promise for high-speed applications. Nonetheless, certain technical constraints have hindered their widespread adoption in high-speed scenari.

Notably, their power factor lags behind that of alternative motor types. Furthermore, a conventional rotor geometry poses problems as it generates high ripple and is not suited for the stresses at high speeds.

The ensuing study aims to address these concerns and develop a viable solutions.

1.2 Synchronous reluctance motors

1.2.1 Working principle

1.2.1.1 Switched reluctance motors

The initial version of reluctance motors is the switched reluctance motor, analyzed by T.A. Lipo in [5]. This motor, akin to all variants of reluctance motors, hinges upon a fundamental principle, the minimization of electromagnetic energies. As depicted in 1.b, the angular position of the rotor minimizes the total energy. A torque is then created when the magnetic energy is changing like in 1.a.

(a) high magnetic energy (b) low magnetic energy

Figure 1: Variation of the magnetic energy for two position of the rotor

For such a straightforward motor and given approximations, torque can be readily calculated by differentiating magnetic energy with respect to rotor angle. This yields the torque T in the expression (1) with the following parameters, i the current, n the number of coil turns, θ the rotor angle, l_i the minimum air gap, l_v the air gap length variation, S the rotor surface

$$T(\theta) = \frac{S\mu_0 n^2 i^2 l_v \sin(\theta)}{2(l_v(\cos(\theta)+1)+l_i)^2} \tag{1}$$

To ensure continuous rotation without stalling, multiple coils can be distributed around the rotor. However, this motor type is not commonly employed due to substantial torque fluctuations during rotation (high torque ripple).

1.2.1.2 Synchronous reluctance motors

A remedy to the aforementioned challenge is the adoption of a synchronous reluctance motor (*SynRm*). The operational principle mirrors that of the switched reluctance motor, where fluctuations in electromagnetic energy yield torque. However, in this context, the coils are energized by a three-phase sinusoidal source. This configuration is illustrated in the ensuing Figure:

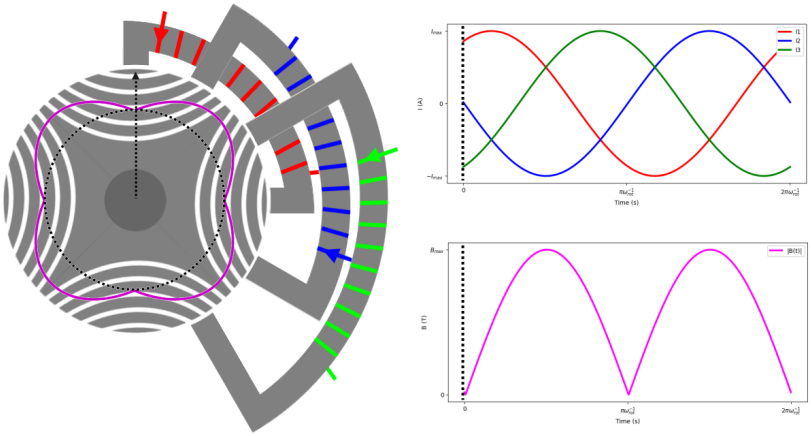

Figure 2: Example of a synchronous reluctance motor

This class of reluctance motor is most prevalent, given its capability to generate substantial torque while maintaining lower torque ripple compared to alternative motor types. With a three-phase excitation spaced at 120°, this motor variety is especially well-suited for industrial applications.

1.2.2 Design criteria for high speed *SynRm*

The forthcoming sections delves into the analysis of a three-phase synchronous reluctance motor tailored for an air compressor application. The motor's specifications bear resemblance to those employed by Z. Kolondzowski in [6], where a permanent magnet motor was the subject of the investigation. The motor adheres to the specifications outlined in the subsequent table.

Criteria	Value
Rotation speed	31500rpm
Rated power	130 kW
Maximum power	252 kw
Maximum torque	80 N.m
Targeted efficiency	96 %
Expected maximum rotor temperature	100°C

Figure 3: Design specification for the *SynRm*

These specified values serves as a reference throughout the study, guiding the motor design process. All of the geometry information on the rotor and stator can be found in the Appendix C.

1.2.3 Existing proposition for high speed *SynRm*

Numerous efforts have been dedicated to achieving elevated rotational speeds in *SynRm* .

One particular rotor configuration utilized by G. Pellegrino in [7] is the transversely laminated design, depicted in Figure 4a. However, employing a rotor geometry tailored for low-speed applications proves ineffective at high speed. To address this limitation, a strategy involving topology optimization has been employed to reshape the rotor to sustain high speeds. This

innovation has been employed by A. Belahcen in [8] and is illustrated in Figure 4b. It is essential to acknowledge that this approach does present challenges, as the modified geometry leads to a noticeable reduction in torque output.

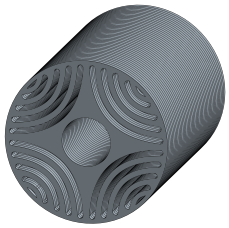

(a) Transversely laminated rotor

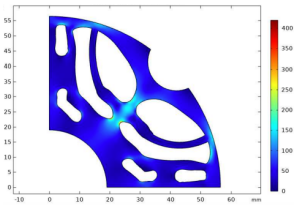

(b) High speed solution [8]

Figure 4: Transversely laminated rotor and solution for high speed application

An alternate approach involves the implementation of an axially laminated rotor, as depicted in Figure 5a. At lower speeds, the conventional method of attaching the rotor components is via bolts. However, at higher speeds, these bolts are inadequate in terms of structural integrity, rendering the low-speed attachment approach impractical. An alternative solution proposed by K. Grace in [9] is the utilization of a carbon fiber sleeve to secure the rotor components. While this method facilitates high-speed rotation, it does lead to a reduction in the motor's maximum torque due to the increased air gap. Furthermore the potential for corrosion between the metal and carbon fiber is high, consequently impacting the motor's operational lifespan.

An additional avenue involves the application of vacuum brazing to unite two distinct metals, one magnetic and the other non-magnetic, into a single solid rotor. This approach, employed by V. Abramenko in [10], is well-suited for high-speed applications while still preserving the motor's maximal torque output. However, a primary challenge with this rotor configuration pertains to the intricacies of manufacturing, as the components must be manufactured to precise dimensions to ensure successful assembly.

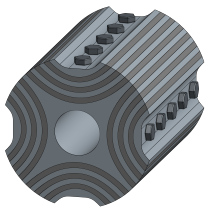

(a) Axially laminated rotor

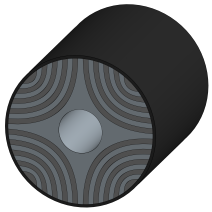

(b) High speed sleeve solution

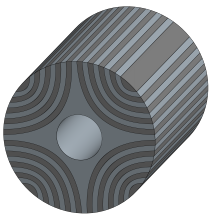

(c) High speed vacuum brazing solution

Figure 5: Axially laminated rotor and solution for high speed application

1.3 Multi material rotor made by powder metallurgy

As observed in the preceding section, a promising avenue involves the assembly of two disparate metals to create a unified solid metal structure capable of withstanding the substantial stresses induced by rotational forces. Given the intricate nature of achieving this assembly through vacuum brazing, an alternative manufacturing technique is proposed.

1.3.1 Powder layering technology

The manufacture of metal powder parts is a well-established procedure that has been employed for numerous years to fabricate intricate components. However, this technique exhibits limited

flexibility, as it necessitates the creation of molds for shaping, a process that is both time-consuming and costly. Additionally, traditional implementations of this method typically yield parts composed of a single material.
In response to these challenges, Grid Logic introduced a novel manufacturing process [11]. This innovative approach involves the layering of multiple layers comprising of ceramic (as support) and metal powders, superposed upon each other to form the final component, as illustrated in Figure 6.

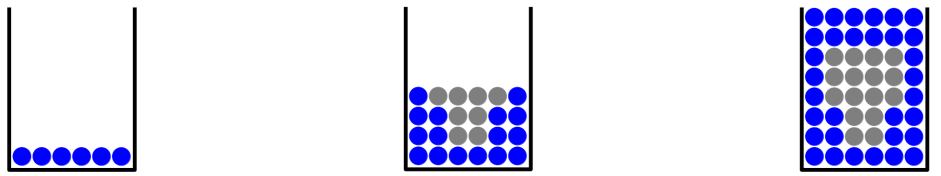

First layer Middle layer Final layer

Figure 6: Process used by Grid Logic

1.3.2 Choice of post processing for the part

Upon the stacking of layers of metal and ceramic powders, the consolidation of the metal is imperative. This fusion can be achieved through various methods, contingent upon the selected materials.

The initial technique involves the utilization of a controlled atmosphere oven to prevent corrosion. The temperature is elevated near to the metals' melting point. At this elevated temperature, the metal powder coalesces, resulting in the formation of a singular, solid metal block. Given that ceramics remain unaltered by the temperature, the part retains a similar shape.

The second method entails the deployment of a high-pressure oven (HIP). Due to the pressurized environment (100 MPa), lower temperatures can be employed, allowing for material properties of the two metals to harmonize, thereby promoting a robust bond between them. The application of pressure accelerates the densification process.

In both scenari, a slight alteration in the part's geometry occurs during the thermal cycle. This phenomenon arises from the composition of the material, as it is made of powder, comprising small spheres with a maximum packing efficiency described as follow, with V_s the volume of two spheres of radius r and V the volume of the cube in which the two spheres fit as compactly as possible.

$$\frac{V_s}{V} = \frac{\frac{8}{3}\pi r^3}{\left(\frac{4r}{\sqrt{3}}\right)^3} = 0.68 \tag{2}$$

Thus to reach a dense final product, a volume reduction of 32% is anticipated.
Regrettably, the manufacturing documentation does not offer further insight into the potential impact of this volume alteration on the part's performance.

Since the rotor will be made of two materials the decision was made to investigate the HIP process due to its capability to effectively post-process components composed of dissimilar ma-

terials.

1.3.3 Choice of the materials

The selection of materials is guided by several discerning criteria. One of the materials must exhibit favorable magnetic attributes, characterized by high initial permeability and a low coercive field. The other metal should possess no magnetic properties, exemplified by a relative permeability of 1. Furthermore, these two metals must demonstrate close mechanical properties and thermal expansion coefficients to enable the powder processing building technique. Chemical compatibility is imperative, with no reactions occurring between the metals to prevent self-corrosion of the final part. Additionally, both metals must be available in powdered form to facilitate the manufacturing of the rotor.

Only a limited range of materials fulfills these stringent criteria. Inconel 625, a non-magnetic metal, was chosen due to its alignment with all previously stipulated requirements. This choice was also made by V. Abramenko as documented in [12] when building the prototypes, ensuring comparable results.
For the magnetic component, the initial objective was to employ structural steel (S235), akin to V. Abramenko's approach. However, as powdered structural steel was unavailable, an alternative selection was necessitated, leading to the adoption of 3% silicon steel. This choice comes from its similarity in material properties to Inconel 625 and its availability in powder form. A notable advantage of silicon steel over structural steel is its elevated silicon content, which reduces conductivity and consequentially mitigates rotor losses. Detailed material specifications are provided in Appendix B.

2 Investigation of the bond between 2 metals in powder metallurgy

With the manufacturing processes of the rotor now established, it is important to have a better comprehension of the mechanical characteristics of the part created. This section is dedicated to the interface between the two utilized metals to build the the rotor, Inconel and 3% Silicon Steel.

In the course of this investigation, the interface between the two metals is presumed to be perfectly planar on the macroscale. It should be noted that in actual parts, the metal powder could potentially exhibit minor mixing during the layering procedure, thus deviating from this idealized flat interface. This simplifying assumption is adopted to streamline the comprehension of the interface characteristics.

2.1 Diffusion bonding due to the HIP process

Once the layering of metal powder is finished and forms the part, the step of consolidation ensues, facilitated by the deployment of Hot Isostatic Pressing (HIP). Elaborate explanation of this process is documented by H.V. Atkinson [13] in the context of single-material solids. In our scenario, the HIP procedure spans a duration of 8 to 12 hours, operating under a pressure of 100 MPa and within a temperature range of 950°C to 1100°C.

Throughout this process, two simultaneous phenomena are happening. The initial process concerns the densification of the material, resulting in a reduced porosity. The second process involves diffusion at the boundary between the two distinct materials, leading to a stronger bond between the metals.

2.1.1 Densification process

Throughout the Hot Isostatic Pressing (HIP) process, the fastest phenomenon encountered is the densification of the material. This process works by transforming small metal spheres, approximately $50\mu m$ in diameter, into a solid and compact metal structure. This technique is detailed by C. Cai in [14]. The process starts by subjecting the initial metal powder part to elevated temperatures, approaching the melting point. During this phase, the metal particles gradually merge together. Following this initial period, the pressure within the oven is elevated, serving to eliminate the remaining porosity within the part. The pressure and temperature cycle employed during this process is graphically depicted below.

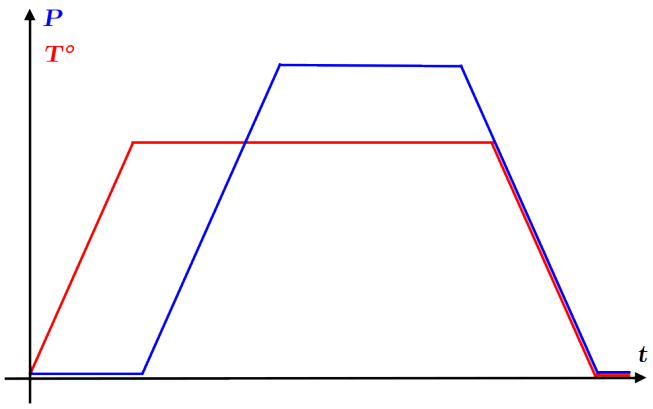

Figure 7: Temperature and pressure cycle of the HIP process

Ordinarily, the temperature for a HIP cycle is chosen in tandem with the pressure. These parameters jointly determine the duration of the HIP cycle, as illustrated in Figures from J.K. Tien's work [15], presented below.

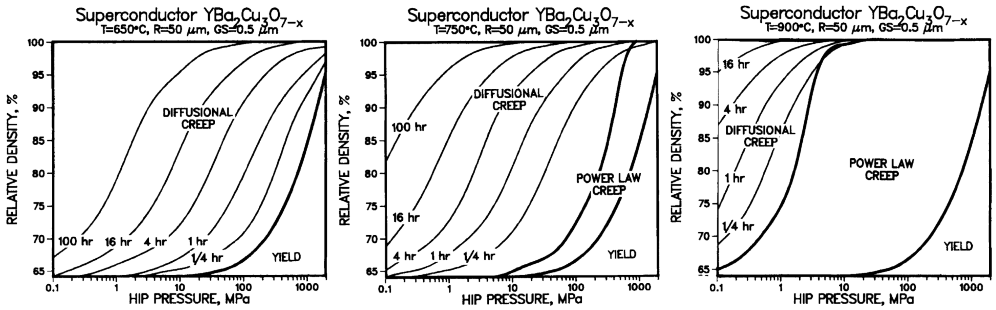

Figure 8: Densification as a function of pressure and time for different temperatures

Consequently, a variety of temperature and pressure combinations can be employed to regulate the time spent within the oven, ultimately determining the desired final density.
In the case of the rotor the fabricated part consists of two distinct materials. Thus, the heat cycle temperature must be selected such that the two materials exhibit an equivalent Young's modulus. This ensures that when the metal powder are compressed, both types of powder deform in a identical manner. The determination of this temperature involves plotting a graph illustrating temperature against Young's modulus. The intersection of the curves for the two materials establishes the temperature for the HIP process, as demonstrated in the graph below.

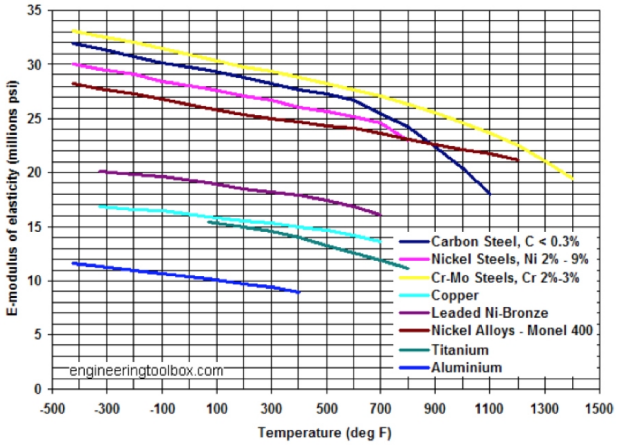

Figure 9: Young's modulus as a function of temperature, adapted from [16]

Hence, with a temperature of approximately 900°C as illustrated in the preceding Figure for similar materials such as Carbon Steel and Monel 400, the duration of densification is below 15 minutes.

Considering that the overall HIP process duration ranges from 8 to 12 hours, the majority of this duration is allocated to the diffusion process between the two distinct materials.

2.1.2 Diffusion process

The phenomenon of diffusion between two distinct metals is a well-established process that has been extensively explored across various metal combinations, as demonstrated by K. Arioka's investigation [17] involving carbon steel and nickel. To simplify the study of this diffusion

process, is is assumed that the initial contact between the dissimilar metals is established during the initial densification phase of the HIP process, and that the diffusion process is symmetry. Consequently, a one-dimensional Fick diffusion law explained by J. Crank in [18] is applicable along the axis perpendicular to the initial interface, as depicted in Equation (1), where c represents the concentration of one material, and $D(T^\circ)$ denotes the diffusion coefficient.

$$\frac{dc}{dt} - D(T^\circ)\nabla^2 c = 0 \tag{3}$$

Considering the temperature-dependent nature of the diffusion coefficient for solid-to-solid diffusion, the Arrhenius equation, as formulated by S. Arrhenius [19], is employed. The diffusion coefficient is represented as follows, with D_0 signifying the initial diffusion coefficient, E_a denoting the activation energy, and R being the universal gas constant.

$$D(T^\circ) = D_0 \exp\left(-\frac{E_a}{RT^\circ}\right) \tag{4}$$

The values of D_0 and E_a are subsequently adjusted to fit experimental data. For our particular case, the obtained values are as follows:

$$D_0 = 2.8 \times 10^{-13}, \mathrm{m}^2 \cdot \mathrm{s}^{-1} \tag{5}$$

$$E_a = 88.8\mathrm{kJ} \cdot \mathrm{mol}^{-1} \tag{6}$$

With these values, the diffusion equation can be solved. Rather than resorting to numerical solutions, an analytical solution explained in [20] is achievable for a fixed initial condition $c_0(x)$ and a length L, this length should surpass the diffusion length, it represents the length where the concentration is allowed to vary.

$$c(x,t) = \frac{2}{L}\sum_{n=1}^{\infty} e^{-\left(\frac{n\pi D(T)}{2L}\right)^2 t} \sin\left(\frac{n\pi x}{L}\right) \int_0^L c_0(x) \sin\left(\frac{n\pi x}{L}\right), dx \tag{7}$$

These equations enable the representation of the concentration over the bond across varying temperatures and durations of the HIP cycle, as illustrated below.

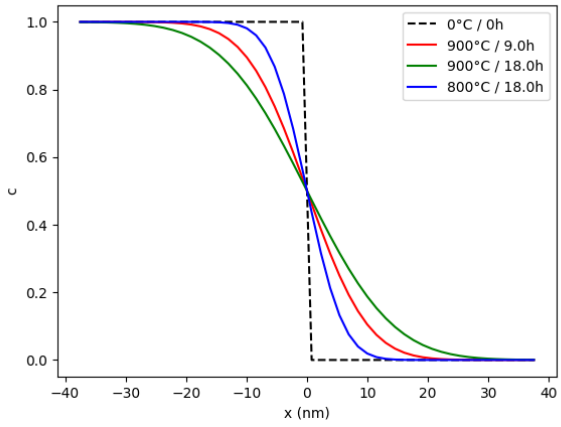

Figure 10: Evolution of the concentration of one material

Ultimately, the material concentrations can be converted into volume fractions, a it is necessary for subsequent analysis. This transformation is achieved via the following equations, where f_I and f_s represent the volume fraction of Inconel and silicon steel, respectively.

$$f_I = \frac{c_I}{c_I + c_s \frac{\rho_I}{\rho_s}} \tag{8}$$

$$f_s = \frac{c_s}{c_s + c_I \frac{\rho_s}{\rho_I}} \tag{9}$$

Here, c_s and c_I denote the concentration of silicon steel and Inconel, subject to the following equation.

$$c_I + c_s = 1 \tag{10}$$

2.2 Mechanical behavior of the bond

Having obtained an understanding of the distribution of mass around the interface for each material, it becomes feasible to deduce the material properties through the implementation of homogenization on planes parallel to the interface. This is done by employing a self-consistent approach with spherical inclusions, this is a preliminary assumption due to the absence of fabricated samples, rendering the inclusion shape uncertain.

To obtain equivalent mechanical properties, the following expression explained by M. Lévesque in [21] is employed:

$$\sum_i f_i \left(\mathbb{I} + \mathbb{S}_i^E : \tilde{\mathbb{C}}^{-1} : (\mathbb{C}_i - \tilde{\mathbb{C}}) \right)^{-1} = \mathbb{I} \tag{11}$$

With f_i the volume fraction $\mathbb{C}_i$ the stiffness tensor of component i and $\tilde{\mathbb{C}}$ the homogenized stiffness tensor defined as follows for a isotropic material.

$$\mathbb{C} = \frac{E}{(1+\nu)(1-2\nu)} \begin{pmatrix} 1-\nu & \nu & \nu & 0 & 0 & 0 \\ \nu & 1-\nu & \nu & 0 & 0 & 0 \\ \nu & \nu & 1-\nu & 0 & 0 & 0 \\ 0 & 0 & 0 & \frac{1-2\nu}{2} & 0 & 0 \\ 0 & 0 & 0 & 0 & \frac{1-2\nu}{2} & 0 \\ 0 & 0 & 0 & 0 & 0 & \frac{1-2\nu}{2} \end{pmatrix} \tag{12}$$

And $\mathbb{S}_i^E$ the Eshlby tensor for the component i defined for round inclusions as

$$\mathbb{S}^E = \frac{1}{15(1-\nu)} \begin{pmatrix} 7-5\nu & 5\nu-1 & 5\nu-1 & 0 & 0 & 0 \\ 5\nu-1 & 7-5\nu & 5\nu-1 & 0 & 0 & 0 \\ 5\nu-1 & 5\nu-1 & 7-5\nu & 0 & 0 & 0 \\ 0 & 0 & 0 & 8-10\nu & 0 & 0 \\ 0 & 0 & 0 & 0 & 8-10\nu & 0 \\ 0 & 0 & 0 & 0 & 0 & 8-10\nu \end{pmatrix} \tag{13}$$

Then, equation (11) can be solved to determine $\tilde{\mathbb{C}}$, consequently enabling the calculation of the homogenized material parameters. In our case, a numerical approach was adopted to solve this equation. The resultant material parameters can be approximated using a hyperbolic tangent function, facilitating their integration into finite element software, for instance.

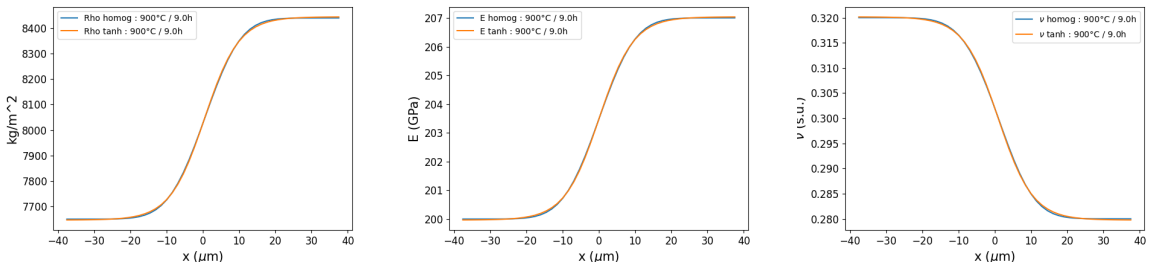

Figure 11: Evolution of the density, Young's modulus, and Poisson's ratio across the interface

Ultimately, a characteristic bond length can be determined. This involves locating points on each side of the interface where the concentration is reduced by 2.5% (ensuring that 95% of the interface is captured within the range). Subsequently, the distance between these two points can be measured. In our case, the interface length was calculated to be $40.9\mu m$.

2.3 Using the mechanical behavior of the bond for larger scale parts

With the material parameters of the interface now determined, an initial approach for their application might involve directly incorporating these results into a finite element simulation, as exemplified in the following images.

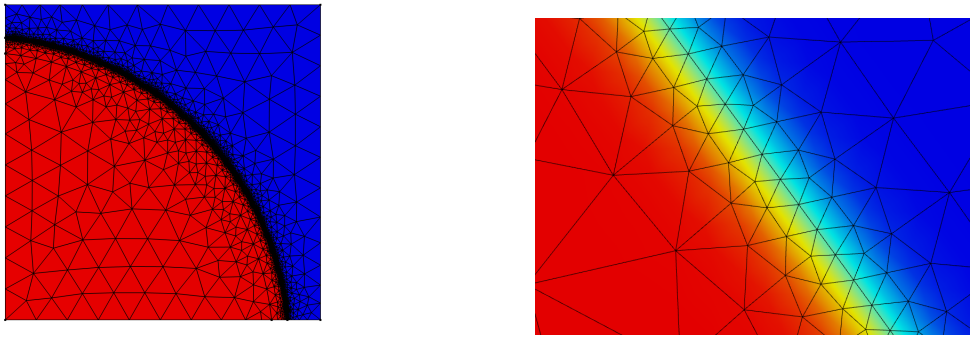

Model as an example

Zoom on the interface

Figure 12: Example of a finite element simulation on a part with an interface

Due to the substantial ratio of part size to interface size (approximately 1000), mesh refinement around the interface is necessary. However, this approach introduces challenges. For intricate components, it results in complicated meshes, which become time-consuming to solve. Moreover, even with fine meshing, the material parameters do not remain constant within a single element, thus deviating from the assumptions of the finite element model. Lastly, considering that the interface is comprised of two materials with distinct yield strengths, thus predicting the point at which the interface enters its plasticity domain becomes challenging.
Consequently, the direct utilization of material parameters within a finite element model is not straightforward. Instead, a strategy involving a part with discontinuous materials was adopted, employing regular-sized elements and nodes along the interface. By doing so, the nodal stress values can be employed in conjunction with a new load space surface to define a safety ratio.

2.3.1 Homogeneous fields over the bond

Defining as safety criteria is most easily done by using the stress field to define a load surface in a $(\sigma_{xx}, \sigma_{yy})$ space, it was chosen to employ the stress at the interface to establish the criterion.

Initially, a change of coordinate system is necessary, as the (e_x, e_y) orientation is not always aligned with the principal coordinate system of the interface, the angle between those two coordinate system is Θ, as illustrated below.

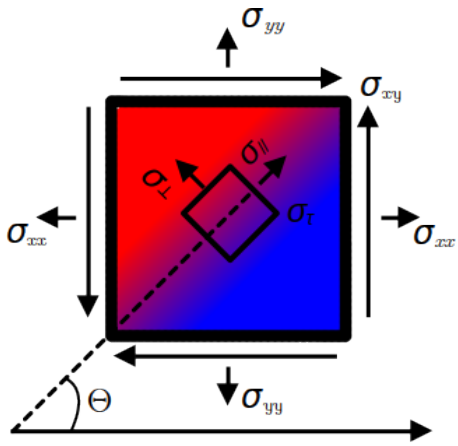

Figure 13: Part coordinate system and interface principal coordinate system

The transformation between these two coordinate systems is achieved through a simple rotation matrix defined as

$$\begin{pmatrix} \cos(\Theta) & -\sin(\Theta) \\ \sin(\Theta) & \cos(\Theta) \end{pmatrix} \begin{pmatrix} \sigma_{xx} & \sigma_{xy} \\ \sigma_{xy} & \sigma_{yy} \end{pmatrix} \begin{pmatrix} \cos(\Theta) & \sin(\Theta) \\ -\sin(\Theta) & \cos(\Theta) \end{pmatrix} = \begin{pmatrix} \sigma_{//} & \sigma_{\tau} \\ \sigma_{\tau} & \sigma_{\perp} \end{pmatrix} \tag{14}$$

The idea is then to utilize the stresses at the interface and apply them to an equivalent small-scale interface where no approximations are introduced. The first step is to define the boundary conditions.

The stresses parallel to the interface ($\sigma_{//}$) are discontinuous due to the changing material parameters across the interface. Despite this, due to the continuity of the displacement field, the strain field parallel to the interface ($\epsilon_{//}$) remains continuous. Conversely, the remaining components of the stress tensor ($\sigma_{\perp}$ and σ_{τ}) are continuous. These results can be validated using finite element simulations, observing each component across the interface for both continuous and discontinuous material parameter interfaces, as depicted below.

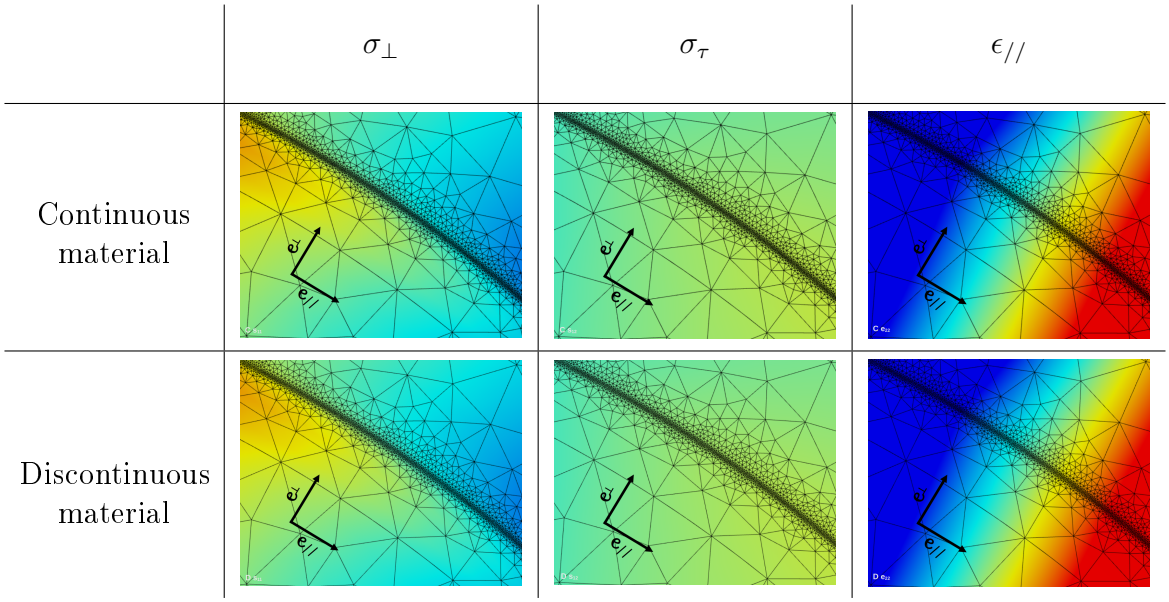

In the end, given the continuity of these fields and the fact that the interface size is significantly

smaller than the part geometry, the stress and strain fields can be assumed to be locally homogeneous over the interface.
However, the $\epsilon_{//}$ field is not directly attainable when plotting a load space. It needs to be calculated from the discontinuous $\sigma_{//}$. A convenient value to obtain for this purpose is the maximum of $\sigma_{//}$, denoted as $\sigma_{//\max}$. Using the local linearity and homogeneity, Hooke's law can be applied locally, resulting in:

$$\epsilon_{//} = \frac{1+\nu_{\max}}{E_{\max}}\sigma_{//\max} - \frac{\nu_{\max}}{E_{\max}}(\sigma_{//\max} + \sigma_{\perp}) \tag{15}$$

Where $E_{\max}$ is the higher Young's modulus of the two materials, and $\nu_{\max}$ is the corresponding Poisson's ratio.
Consequently, these three homogeneous fields can be deduced from the components of the stress tensor.

2.3.2 Calculating the stresses in the bond

With the stress and strain now understood around the interface, the strain in the homogenized material can be calculated. For this purpose, a new problem is formulated with constant boundary conditions, as illustrated below.

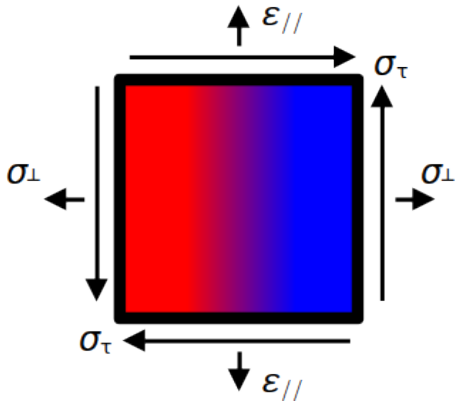

Figure 14: Problem to solve with two different materials in red and blue

2.3.2.1 Homogenized Strain

The objective here is to determine the strain in the part for all possible stress combinations. The strain in the $\epsilon_{//}$ direction is already known by the boundary conditions, as defined before this stress is homogeneous.
For the other two strain components, Hook's law is employed, given that the material is locally linear, isotropic, and homogeneous. As such, the strain can be expressed as follows:

$$\epsilon_{\perp} = \frac{1+\nu(x)}{E(x)}\sigma_{\perp} - \frac{\nu(x)}{E(x)}(\sigma_{//}(x) + \sigma_{\perp}) \tag{16}$$

$$\epsilon_{\tau} = \frac{1+\nu(x)}{E(x)}\sigma_{\tau} \tag{17}$$

Where

$$\sigma_{//}(x) = \frac{E(x)\nu(x)}{(1+\nu(x))(1-\nu(x))}(\epsilon_{\perp} + \epsilon_{//}) + \frac{E(x)}{1+\nu(x)}\epsilon_{//}$$

Subsequently, these equations are combined to deduce the strain within the interface:

$$\epsilon_{//} = \frac{1+\nu_{\max}}{E_{\max}}\sigma_{//\max} - \frac{\nu_{\max}}{E_{\max}}(\sigma_{//\max} + \sigma_{\perp}) \tag{18}$$

$$\epsilon_{\perp} = \sigma_{\perp}\frac{1-\nu(x)^2}{E(x)} - \nu(x)\left(\frac{1+\nu_{\max}}{E_{\max}}\sigma_{//\max} - \frac{\nu_{\max}}{E_{\max}}(\sigma_{//\max} + \sigma_{\perp})\right) \tag{19}$$

$$\epsilon_{\tau} = \frac{1+\nu(x)}{E(x)}\sigma_{\tau} \tag{20}$$

2.3.2.2 Stresses in the Inclusions

Now that the strain tensor is understood within the interface, a criterion needs to be established to determine whether the deformation field will lead to plasticized regions. To achieve this, the stress within grains that have diffused are calculated, assuming that their strain field follows the homogeneous strain field. To do this, the Hook's law is applied once more, but this time to the material grains that have diffused into the other material, using their respective material properties.

$$\begin{aligned}
\sigma^i_{//} &= \frac{E_i\nu_i}{(1+\nu_i)(1-\nu_i)}(\epsilon_{\perp} + \epsilon_{//}) + \frac{E_i}{1+\nu_i}\epsilon_{//} \\
\sigma^i_{\perp} &= \frac{E_i\nu_i}{(1+\nu_i)(1-\nu_i)}(\epsilon_{\perp} + \epsilon_{//}) + \frac{E_i}{1+\nu_i}\epsilon_{\perp} \\
\sigma^i_{\tau} &= \frac{E_i}{1+\nu_i}\epsilon_{\tau}
\end{aligned} \tag{21}$$

Here, i denotes either the Inconel or the Silicon steel materials.
Then, the von Mises equivalent stress can be calculated for each set of material parameters:

$$\sigma^i_{\mathrm{vm}} = \sqrt{(\sigma^i_{\perp})^2 - \sigma^i_{\perp}\sigma^i_{//} + (\sigma^i_{//})^2 + 3(\sigma^i_{\tau})^2} \tag{22}$$

2.3.3 Defining a new safety ratio

Now that the equivalent stresses have been computed for both materials, a safety ratio can be calculated by dividing the von Mises stresses by the yield strength (Y_s) of each material. The safety ratio is defined as follows:

$$S_r = \max_{\mathrm{bond}}\left(\max\left(\frac{\sigma^{\mathrm{Inconel}}_{\mathrm{vm}}}{Y^{\mathrm{Inconel}}_s}, \frac{\sigma^{\mathrm{FeSi}}_{\mathrm{vm}}}{Y^{\mathrm{FeSi}}_s}\right)\right) \tag{23}$$

This value can be used to determine if the bond is still within the elastic domain.
Since calculating this safety ratio from a finite element simulation is not straightforward, a decision was made to calculate an equivalent load surface in the $(\sigma_{xx}, \sigma_{yy})$ plane. This approach takes all possible loading cases into account and can be directly used in finite element software. The procedure for calculating this load space is as follows, for each load angle Γ defined in (24), the norm of the stress vector N_σ defined in 25 is incrementally increased until the safety ratio becomes equal to one. This process is repeated for each orientation of the bond, and the minimum value is retained for that load angle. This calculation is then repeated for every angle Γ. Once completed, the results can be plotted in the σ_{xx} σ_{yy} plane, resulting in a new load space as follow.

$$\Gamma = \mathrm{atan2}(\sigma_{xx}, \sigma_{yy}) \tag{24}$$

$$N_\sigma = \sqrt{\sigma_{xx}^2 + \sigma_{yy}^2} \tag{25}$$

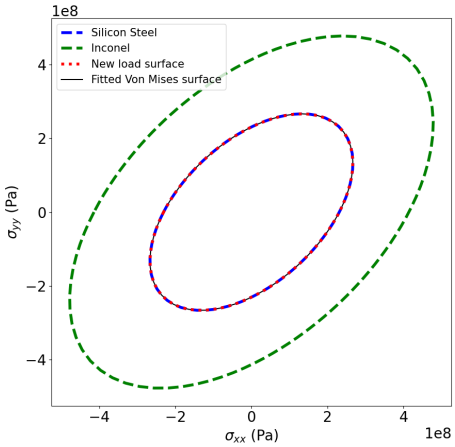

Figure 15: New load space

Implementing this load space directly in finite element software can be challenging. Thus, a von-Mises surface was fitted within the new load space. Consequently, the von Mises stress obtained from the finite element model can be divided by the new yield stress, resulting in the safety ratio for the entire part. In our case, this new yield stress value was 230.9 MPa. This value is very close to the value of the silicon steel, which is expected since the two materials have similar young modulus and Poisson's ratio. For materials with vastly different Young's modulus and the same yield strength, the new load surface differs significantly from both materials, as shown in the following Figure:

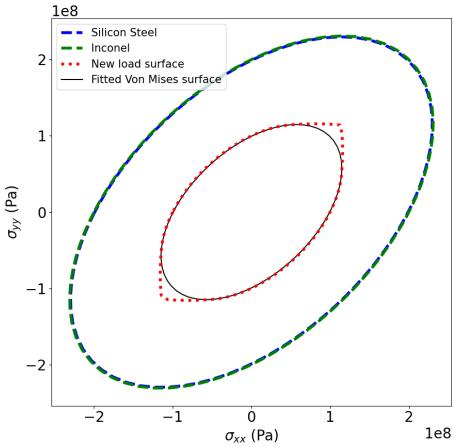

Figure 16: New load space with $E_1 = 200$ GPa, $E_2 = 100$ GPa, and $Y_s^1 = Y_s^2 = 200$ MPa

3 Study of the mechanical behavior of a diffusion bonded rotor

A criteria has been established to assess the structural integrity of a multi-material component and to determine whether it remain within the elastic deformation range. This criterion has been be implemented in each numerical simulation to streamline result visualization. By utilizing this criterion, the robustness of a rotor under various load conditions can effectively be evaluated. In this mechanical analysis, the aspect of fatigue is not be explored, as the primary objective is to test the rotor's ability to withstand a single rotation at its designated high operational speed of 31500 rpm.

Mechanical stresses within a rotor are diverse; however, the focus in the subsequent sections is directed towards the three primary stresses prevalent in rotor structures. The comparison and significance of these stresses has been elucidated by Iruikwu in a study [22] concerning low-speed *SynRm* motors. Nevertheless, in the context of high-speed axially laminated motors, the implications of those stresses are different. Consequently, a new investigation is warranted to comprehensively examine the impact of the stress components present within a high speed rotor.

The three principal stresses in *SynRm* machines encompass the stress induced by rotor rotation, the stress resulting from shaft shrink fitting, and, lastly, the stress arising from thermal expansion since the thermal expansion coefficient is different for each material.

3.1 Theoretical stress analysis in a homogeneous rotor

In this section, the stress distribution within a rotor is examined, considering a rotor made of homogeneous silicon steel and a shaft made of Inconel. The material properties are denoted by subscripts $shaft$ and $rotor$ for Inconel and silicon steel, respectively. It should be noted that the Young modulus and Poisson ratio are considered equal in both material as a simplification but the thermal expansion coefficients are supposed different. Since the rotor's thickness is high the plane strain condition is applied to work in 2D.

3.1.1 Centrifugal stress

Firstly the centrifugal stress experienced by the components is investigated. Figure 17 illustrates the rotor, shaft and the coordinates systems used (cartesian and cylindrical).

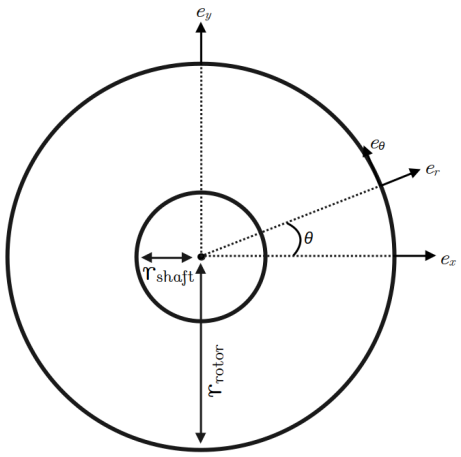

Figure 17: Schematic of the simplified rotor and shaft.

3.1.1.1 Centrifugal stress in the shaft

First, the stress within the shaft is focused on. The rotor and shaft are treated separately as their boundary conditions are different. The following equations governs the behavior of stress and strain inside the shaft, assuming homogeneity, linearity, and continuity of the materials, with λ and ν the lame coefficients.

$$\boldsymbol{\epsilon} = \frac{1}{2}\left(\nabla u + {}^t\nabla u\right) \tag{26}$$

$$\boldsymbol{\sigma} = \lambda \operatorname{tr}(\boldsymbol{\epsilon})\mathbb{I} + 2\mu\boldsymbol{\epsilon} \tag{27}$$

$$\operatorname{div}\boldsymbol{\sigma} + \rho\omega^2 r.e_r = 0 \tag{28}$$

The boundary condition applied to the shaft is given by the following equation with n the vector normal to the surface.

$${}^t n\boldsymbol{\sigma}(r_{shaft}).n = 0 \tag{29}$$

The part is considered as being of infinite length thus the problem is unchanged by translation on the e_z axes. Furthermore a rotation around the e_z axes does not change the problem. Thus, a displacement field can be proposed taking into account those symmetries.

$$u = \begin{pmatrix} u_r(r) \\ 0 \end{pmatrix} \tag{30}$$

Using Equation (26), the strain tensor $\boldsymbol{\epsilon}$ can be calculated:

$$\boldsymbol{\epsilon} = \begin{pmatrix} u_{r,r}(r) & 0 \\ 0 & \frac{u_r(r)}{r} \end{pmatrix} \tag{31}$$

From $\boldsymbol{\epsilon}$, the stress $\boldsymbol{\sigma}$ can be calculated using the Hooke's law as in equation (27):

$$\boldsymbol{\sigma} = \begin{pmatrix} (\lambda + 2\mu)u_{r,r} + 2\lambda\frac{u_r}{r} & 0 \\ 0 & \lambda u_{r,r} + (\lambda + 2\mu)\frac{u_r}{r} \end{pmatrix} \tag{32}$$

Applying the conservation law (28) to $\boldsymbol{\sigma}$ results in a differential equation:

$$\frac{\rho\omega^2 r}{\lambda+2\mu} = u_{r,rr} + \frac{1}{r}u_{r,r} - \frac{1}{r^2}u_r \tag{33}$$

The solution to this differential equation is given by (34) with A and B integrations parameters.

$$u_r = r^3\frac{\rho\omega^2}{8(\lambda+2\mu)} + Ar + \frac{B}{r} \tag{34}$$

For the solution to remain bonded at $r = 0$, B si set to 0. Applying the boundary condition at $r = r_{shaft}$ enables the determination of the constant A, leading to the final result with E the young modulus and ν the Poisson ratio :

$$u_r^{shaft} = \frac{1-\nu}{8E}\rho\omega^2 r_{shaft}^3\left((3+\nu)\frac{r}{r_{shaft}} - (1+\nu)\left(\frac{r}{r_{shaft}}\right)^3\right) \tag{35}$$

From the displacement field u, the stress $\boldsymbol{\sigma}$ can be calculated using Equation (32):

$$\sigma_{rr}^{shaft} = \frac{3+\nu}{8}\rho\omega^2 r_{shaft}^2\left(1 - \left(\frac{r}{r_{shaft}}\right)^2\right) \tag{36}$$

$$\sigma_{\theta\theta}^{shaft} = \frac{3+\nu}{8}\rho\omega^2 r_{shaft}^2\left(1 - \frac{1+3\nu}{3+\nu}\left(\frac{r}{r_{shaft}}\right)^2\right) \tag{37}$$

3.1.1.2 Centrifugal forces in the rotor

The analysis for the rotor follows a similar approach, albeit with different boundary conditions due to the presence of a hole. The new boundary conditions are given by:

$$\begin{aligned} {}^t n\boldsymbol{\sigma}(r_{shaft}).n = 0 \\ {}^t n\boldsymbol{\sigma}(r_{rotor}).n = 0 \end{aligned} \tag{38}$$

Solving Equation (33) for the rotor by employing the solution form equation (34) with coefficients A and B determined by the new boundary conditions, results in

$$u_r^{rotor} = \frac{(3+\nu)(1-\nu)}{8E}\rho\omega^2 r_{rotor}^2 r\left(1 + \left(\frac{r_{shaft}}{r_{rotor}}\right)^2 + \frac{1+\nu}{1-\nu}\left(\frac{r_{shaft}}{r}\right)^2 - \frac{1+\nu}{3+\nu}\left(\frac{r}{r_{rotor}}\right)^2\right) \tag{39}$$

The stress tensor $\boldsymbol{\sigma}$ for the rotor can be determined using Equation (32):

$$\sigma_{rr}^{rotor} = \frac{(3+\nu)}{8}\rho\omega^2 r_{rotor}^2\left(1 + \left(\frac{r_{shaft}}{r_{rotor}}\right)^2 - \left(\frac{r_{shaft}}{r}\right)^2 - \left(\frac{r}{r_{rotor}}\right)^2\right) \tag{40}$$

$$\sigma_{\theta\theta}^{rotor} = \frac{(3+\nu)}{8}\rho\omega^2 r_{rotor}^2\left(1 + \left(\frac{r_{shaft}}{r_{rotor}}\right)^2 + \left(\frac{r_{shaft}}{r}\right)^2 - \frac{1+3\nu}{3+\nu}\left(\frac{r}{r_{rotor}}\right)^2\right) \tag{41}$$

3.1.1.3 Representation

Having obtained the stress fields for the shaft and rotor, the von Mises equivalent stress can be obtained as defined by equation (42). Visualization and representation of the stress distribution, as depicted in Figure 18.

$$\boldsymbol{\sigma}_{vm} = \sqrt{\frac{3}{2}\left(\boldsymbol{\sigma}^{dev} :^{t} \boldsymbol{\sigma}^{dev}\right)} \tag{42}$$

Where $\boldsymbol{\sigma}^{dev}$ is the stress deviator tensor, given by:

$$\boldsymbol{\sigma}^{dev} = \boldsymbol{\sigma} - \mathbb{I}\frac{\mathrm{tr}(\boldsymbol{\sigma})}{2} \tag{43}$$

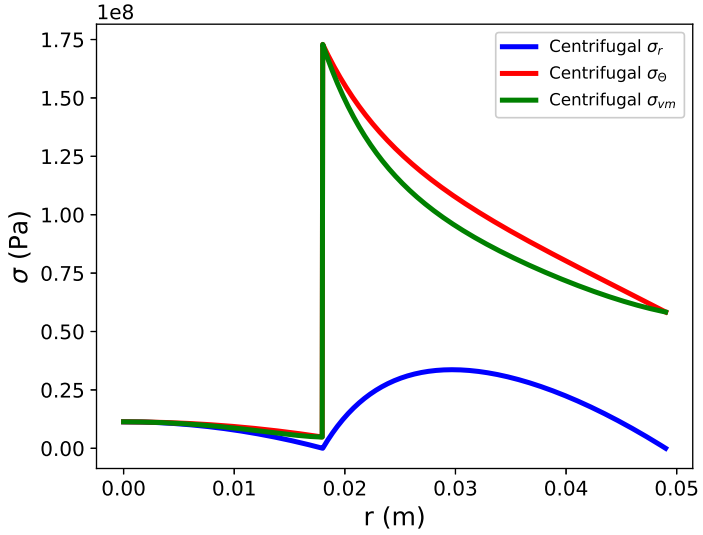

Figure 18: Stress due to the rotation of the rotor

3.1.2 Stresses from shrink fitting

To transmit torque from the rotor to the shaft, the shrink fitting method is chosen at first. This approach, commonly employed in low-speed motors as in [22] by D. Iruikwu, provides a simple and reliable attachment of the rotor to the shaft.

3.1.2.1 Stress calculation

First, the stress within the shaft is analyzed when external pressure is applied. The problem is defined by the following equations :

$$\boldsymbol{\epsilon} = \frac{1}{2}\left(\nabla u +^{t} \nabla u\right) \tag{44}$$

$$\boldsymbol{\sigma} = \lambda\,\mathrm{tr}(\boldsymbol{\epsilon})\mathbb{I} + 2\mu\boldsymbol{\epsilon} \tag{45}$$

$$\mathrm{div}\,\boldsymbol{\sigma} = 0 \tag{46}$$

And the boundary condition:

$$^{t}n.\boldsymbol{\sigma}.n = P \tag{47}$$

Symmetry and invariance considerations lead to a stress tensor form:

$$\boldsymbol{\sigma} = \begin{pmatrix} \sigma_{rr}(r) & 0 \\ 0 & \sigma_{\theta\theta}(r) \end{pmatrix} \tag{48}$$

The strain tensor $\boldsymbol{\epsilon}$ can then be calculated using the hypotheses of plain strain :

$$\boldsymbol{\epsilon} = \begin{pmatrix} \frac{1}{E}\sigma_{rr} - \frac{\nu}{E}\sigma_{\theta\theta} & 0 \\ 0 & \frac{1}{E}\sigma_{\theta\theta} - \frac{\nu}{E}\sigma_{rr} \end{pmatrix} \tag{49}$$

Using equation (31), an equation relating σ_{rr} and $\sigma_{\theta\theta}$ is found :

$$\sigma_{\theta\theta,r} = -\sigma_{rr,r} \tag{50}$$

Additionally, the conservation equation yields:

$$\sigma_{rr,r} + \frac{1}{r}(\sigma_{rr} - \sigma_{\theta\theta}) = 0 \tag{51}$$

Combining these two equations gives:

$$r\sigma_{rr,rr} + 3\sigma_{rr,r} = 0 \tag{52}$$

This differential equation is solvable using the following solution:

$$\sigma_{rr} = A + \frac{B}{r^2} \tag{53}$$

Applying $\sigma_{\theta\theta}$ relation (50) yields:

$$\sigma_{\theta\theta} = C - \frac{B}{r^2} \tag{54}$$

With the relation (51) A is equal to C. To avoid an infinite value at r=0 B is set to 0. Finally using the boundary conditions it is found that :

$$\sigma_{rr}^{shaft} = P \tag{55}$$

$$\sigma_{\theta\theta}^{shaft} = P \tag{56}$$

A similar analysis can be conducted for the rotor with different boundary conditions:

$$\begin{matrix} {}^t n.\sigma_{rr}(r_{shaft}).n = P \\ {}^t n.\sigma_{rr}(r_{rotor}).n = 0 \end{matrix} \tag{57}$$

Calculating the solution for the rotor, results in:

$$\sigma_{rr}^{rotor} = -\frac{Pr_{shaft}^2}{r_{rotor}^2 - r_{shaft}^2} + \frac{Pr_{shaft}^2 r_{rotor}^2}{r_{rotor}^2 - r_{shaft}^2}\frac{1}{r^2} \tag{58}$$

$$\sigma_{\theta\theta}^{rotor} = -\frac{Pr_{shaft}^2}{r_{rotor}^2 - r_{shaft}^2} - \frac{Pr_{shaft}^2 r_{rotor}^2}{r_{rotor}^2 - r_{shaft}^2}\frac{1}{r^2} \tag{59}$$

Then the interference fit resulting from this contact pressure can be calculated. For this the displacement field from the rotor and the shaft that can be calculated using (49) and (31) is needed

$$\begin{aligned} u_r^{shaft} &= \frac{r_{shaft}(1-\nu)P}{E} \\ u_r^{rotor} &= \frac{r_{shaft}}{E}\left((\nu-1)\frac{Pr_{shaft}^2}{r_{rotor}^2 - r_{shaft}^2} - (1+\nu)\frac{Pr_{rotor}^2}{r_{rotor}^2 - r_{shaft}^2}\right) \end{aligned} \tag{60}$$

The resulting interference δ_{ini} can then be calculated by taking the difference of the two displacement fields :

$$\delta_{ini} = 2\frac{P}{E}\left(\frac{r_{shaft}r_{rotor}^2}{r_{rotor}^2 - r_{shaft}^2}\right) \tag{61}$$

The maximum transferable torque can also be calculated as a function of the contact pressure with γ the friction coefficient and l the length of the rotor.

$$T_{max} = 2\pi r_{shaft}^2 l P \gamma \tag{62}$$

3.1.2.2 Stress representation

The stress distribution can be visualized for a specific transferable torque, such as 8000 N.m, as illustrated in Figure 19. This value of transferable torque will reduce once the rotation and the thermal expansion is added, thus explaining the high initial value of transferable torque.

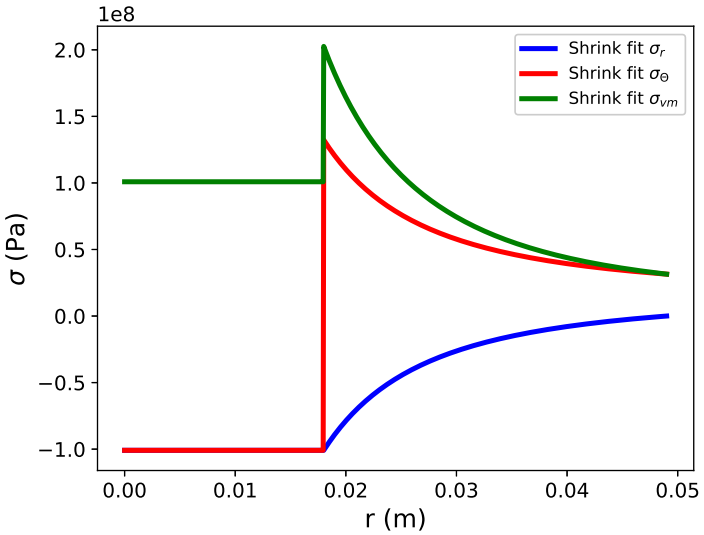

Figure 19: Stress due to shrink fitting of the shaft in the rotor.

3.1.3 Thermal expansion stresses

In comparison to low speed *SynRm* eddy current losses in the rotor are much higher in high speed *SynRm* since the eddy currents are proportional to of the rotational speed and the number of stator slots as shown by H. Ohguchi in [23]. Since the amount of eddy currents generated directly translates to the amount of heat generated in the rotor the thermal expansion is much higher for high speed applications.

In this part the thermal stresses generated by the contact between the shaft and the rotor is looked at. The assumption is made that the rotor material is homogeneous as calculating the stress with complicate shapes is not possible. Furthermore the temperature is considered homogeneous and equal to $100°C$ as it is the objective of the cooling system as in Z. Kolondzovski work in [6].
The thermal stress are due to the different thermal expansion coefficients of the two materials ($13.0 \times 10^{-6}K^{-1}$ and $15 \times 10^{-6}K^{-1}$ for Inconel and Silicon steel respectively). With theses values the thermal stresses should reduce with a temperature increase.

3.1.3.1 Calculation of the thermal stress

The equations of the problem are given, the only difference here is the addition of the thermal expansion law with α_m the thermal expansion coefficient of the material m and T° the temperature.

$$\boldsymbol{\epsilon} = \frac{1}{2}\left(\nabla u + {}^t\nabla u\right) \tag{63}$$

$$\boldsymbol{\sigma} = \lambda \operatorname{tr}(\boldsymbol{\epsilon}^{el})\mathbb{I} + 2\mu\boldsymbol{\epsilon}^{el} \tag{64}$$

$$\operatorname{div}\boldsymbol{\sigma} = 0 \tag{65}$$

$$\boldsymbol{\epsilon} = \boldsymbol{\epsilon}^{el} + \alpha_m \Delta T^\circ \mathbb{I} \tag{66}$$

The problem can be separated in two simpler problems, one thermal part and the elastic part. Thus the elastic problem can be calculated exactly as in the shrink fitting problem since the boundary conditions are the same and the interference δ can be replaced by the difference of the thermal displacement fields at the shaft.

First the thermal displacement field in the shaft and the rotor is calculated, the only difference between the rotor and the shaft being the thermal expansion coefficient.

$$\alpha_m \Delta T^\circ \mathbb{I} = \begin{pmatrix} u_{r,r}^{th} & 0 & 0 \\ 0 & \frac{u_r^{th}}{r} & 0 \\ 0 & 0 & 0 \end{pmatrix} \tag{67}$$

From this equation the displacement field is directly obtained.

$$u_r^{th} = \alpha_m \Delta T^\circ r \tag{68}$$

With this result δ can now calculated.

$$\delta_{th} = (\alpha_{shaft} - \alpha_{rotor})\Delta T^\circ r_{shaft} \tag{69}$$

Then this interference δ_{th} can be taken as the input of the elastic problem that was solved before for shrink fitting.

$$P = \frac{E\Delta T^\circ(\alpha_{shaft} - \alpha_{rotor})}{2}\left(\frac{r_{rotor}^2 - r_{shaft}^2}{r_{rotor}^2}\right) \tag{70}$$

$$\sigma_{rr}^{shaft} = P \tag{71}$$

$$\sigma_{\theta\theta}^{shaft} = P \tag{72}$$

$$\sigma_{rr}^{rotor} = -\frac{Pr_{shaft}^2}{r_{rotor}^2 - r_{shaft}^2} + \frac{Pr_{shaft}^2 r_{rotor}^2}{r_{rotor}^2 - r_{shaft}^2}\frac{1}{r^2} \tag{73}$$

$$\sigma_{\theta\theta}^{rotor} = -\frac{Pr_{shaft}^2}{r_{rotor}^2 - r_{shaft}^2} - \frac{Pr_{shaft}^2 r_{rotor}^2}{r_{rotor}^2 - r_{shaft}^2}\frac{1}{r^2} \tag{74}$$

3.1.3.2 Representation of the stress

The stress can then be plotted for a desired temperature $T°$, for example with 100°C. Care needs to be taken when reading the results, as the calculation has been made with the assumption that the shaft is always in contact with the rotor. This is not always the case as in Figure 20 since the thermal expansion coefficient of the rotor is higher than the one of the shaft. If $\sigma_{\theta\theta}$ is positive, the stress needs to be taken equal to zero.

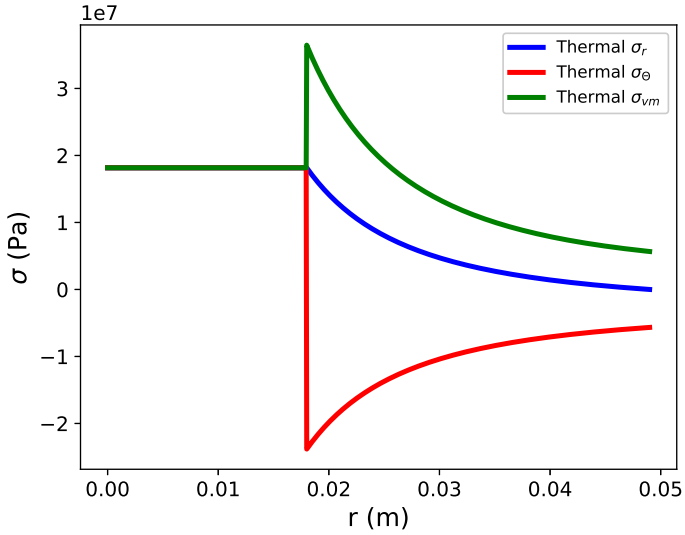

Figure 20: Stress due to thermal expansion

3.1.4 Combination of all the stress

Now that all of the stress in the rotor and shaft have been calculated they can be added to have an idea of the reparation of the stress in the rotor and in the shaft. Each field of the stress tensor is summed using the linearity of the operators that have been used. Then the von Mises stress can be calculated.

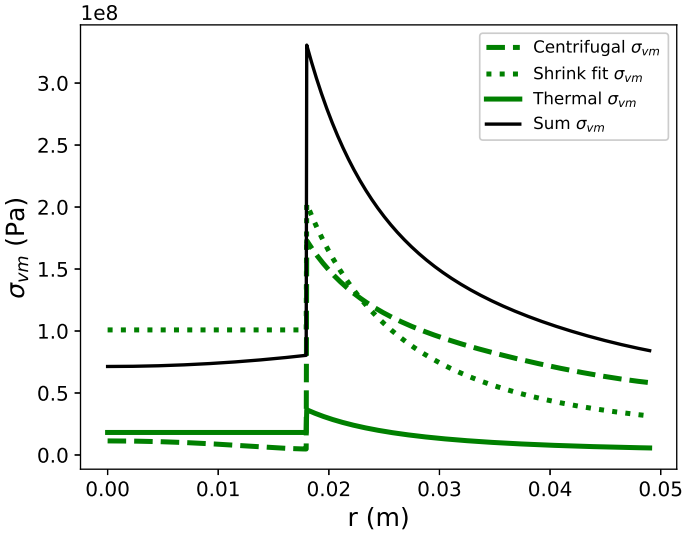

Figure 21: Combination of all of the stresses

With all of the stresses combined the displacement field of the rotor and the axle is calculated,

from this a new interference value can be found using $\delta_{ini}, \delta_{th}, \delta_{rot}$ the values of difference in the displacement fields at the shaft for the shrink fitting , the thermal expansion and the rotation respectively.

$$\delta = \delta_{ini} + \delta_{th} + \delta_{rot} \tag{75}$$

With this new value of the interference between the rotor and the shaft, the transferable torque can be calculated with the help of (62) and (61) . This lead to a new transferable torque value of 500 N.m when taking into account the rotation and thermal expansion with the same initial interference. These equations can be used in the future parts to have as a simple reference for the FE simulations and give a first approximations for parameters value such as the value of the interference needed between the shaft and the rotor.

3.2 Computed stress with a shrink fitted round shaft

3.2.0.1 Numerical model

The theoretical calculations are helpful to get a first approximation of the stresses in the rotor. But these calculation do not take into account the slightly different material parameters in the rotor. Thus a numerical model is created using the Finite Element Method. In this model the two material have different properties as shown in Appendix B's table. Theses properties have been taken from the literature and have not been measured.

The input geometry of the model is as defined in the Figure 22.

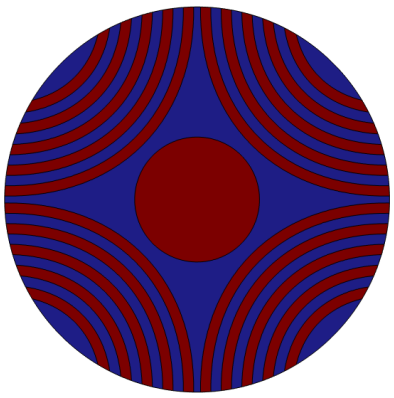

Figure 22: Material domain Silicon Steel, Inconel

As an input parameters the model takes the rotational speed of the rotor and shaft, the interference fit between the rotor and the shaft. The interference fit was chosen so that the transferable torque between the rotor and the shaft was 100 N.m in the worse case. The results are shown using the safety ratio defined in the previous part.

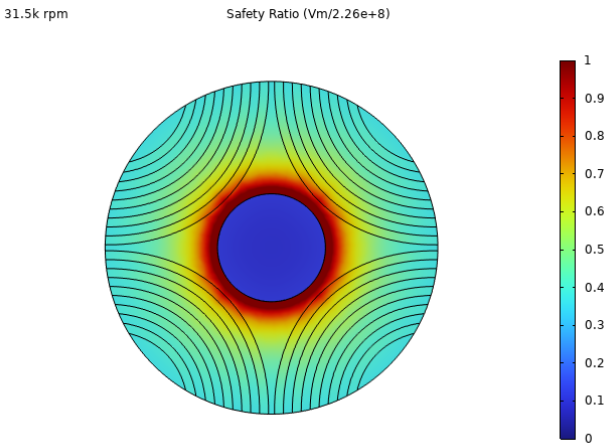

Figure 23: Simulation with stress from the shrink fitting and the rotation

The thermal simulation can not be done at the same time as the mechanical simulation as the computing time of the problem with all of the physics combined is to high. Thus the thermal simulation is done separately. First an electromagnetic time simulation of the rotor and stator is ran with the geometry as defined in Figure 24, This model is defined in more details in Appendix A.

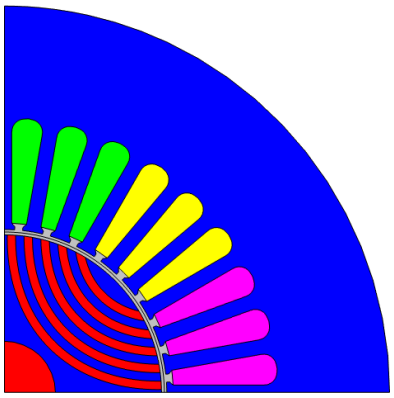

Figure 24: FEM model parts
Silicon steel, Inconel, Air,
Coil 1,Coil 2, Coil 3

This simulation enables us to calculate the power losses in the rotor, then they can be represented for the rotor.

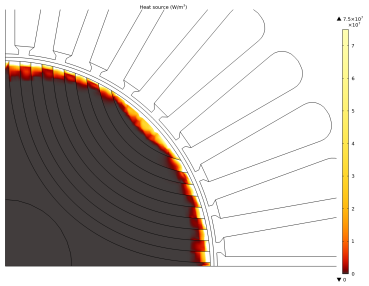

Figure 25: Real magnetic losses

Then those losses are simplified as follow to be taken as an input in a new coupled thermo-mechanical simulation, this enables us to get the mechanical stress in function of time. In this

thermo-mechanical simulation the input power comes from rectangle heat sources, special care was taken so that the total amount of power generated in the electromagnetic simulation and in the thermal simulation was the same. The output power is dissipated through the outside of the rotor using forced convection (with air speed of 150m/s).

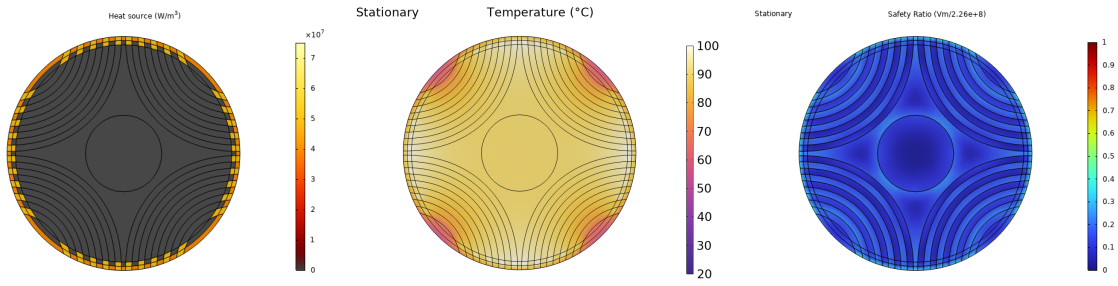

Figure 26: Input losses, final temperature field and stationary stress

Finally the results of the thermo-mecanical simulation and mechanical simulation can be combined to get the full mechanical behavior of the rotor. This is not directly possible in COMSOL, thus a python script was written, this combines the results of both of the simulations by adding each component of $\boldsymbol{\sigma}$ of each simulation. To get the values of $\boldsymbol{\sigma}$ interpolation between the nodal values of the models was used. This interpolation does not always respects the mesh of each model, this is why the results can have strange boundary shapes. This program enables us to add two fields from different models that do not have the same mesh. The results can be seen in the following image.

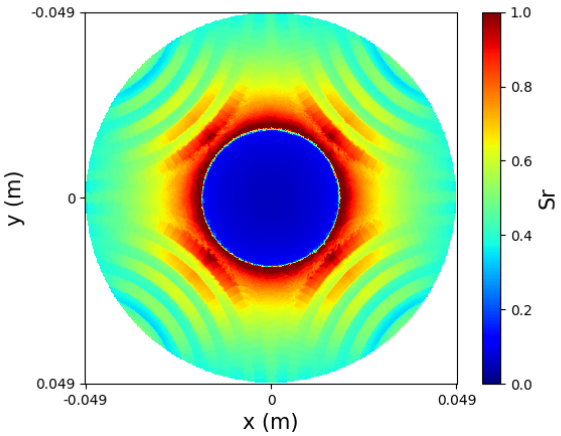

Figure 27: Simulation of the total stress

The values from this last simulation exceed 1 thus, this design does not not work at high speed.

3.3 Stress within a new shaft design

Since the majority of the stress comes from the shaft and the shrink fitting it has been decided to try to change the shaft and not use shrink fitting to assemble the shaft to rotor. The chosen solution is to use a non round shaft that mechanically interferes with the rotor thus enable it to transmit the torque. The new chosen shape is base from two ellipses at 90° from one to an other, tangent line were added to smooth the shape and make it convex. The diameter of the ellipsis was chosen using numerical optimization with the objective of reducing the stress for 500 N.m transmitted torque (five time the rated torque of the motor).

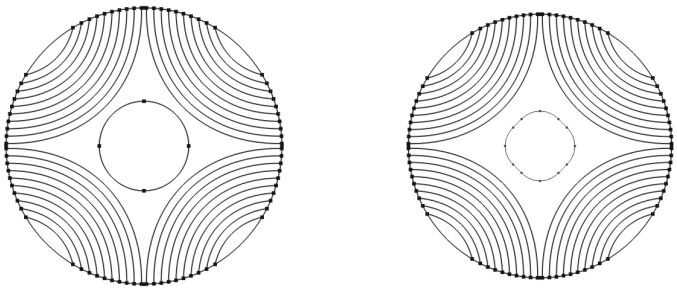

Figure 28: Old shaft geometry and new shaft geometry

The same procedure was used for this new geometry. With (500 N.m) of torque transmitted between the rotor and the shaft.

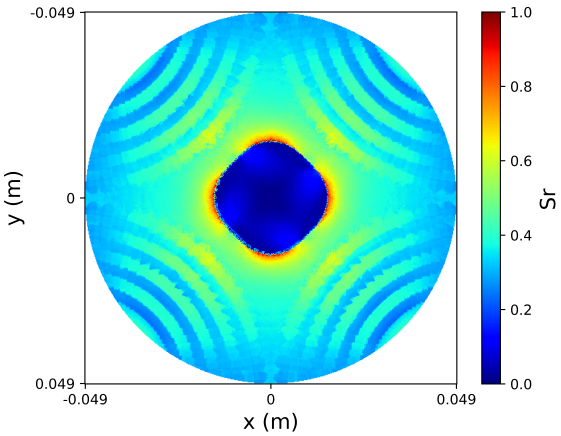

Figure 29: Simulation of the total stress

The stresses are significantly reduced with the new shaft and the maximum safety ratio is 0.9. Thus with this new shaft shape the motor is able to run at full speed and maximum load for a long period of time.

4 Optimization of the geometry of a two-material rotor

4.1 Objectives of the optimization

4.1.1 Basics of optimization

The optimization of mechanical systems involves determining the most favorable configuration or material among various parameter sets. It is difficult to guarantee that exhaustive experimentation will lead to the most optimal solution. An effective approach to circumvent the trial-and-error process is to employ numerical optimization techniques on the model parameters.
The initial step in optimization involves identifying the parameters that can be modified to obtain the optimal solution and defining their respective domains, encompassing the entire problem space. This is mathematically represented by the definition (76) with v as the set of variables.

$$v \in \Omega = \{ \ v \text{ such that } M_{odel}(v) \text{ is defined } \} \tag{76}$$

Next, a cost function C must be formulated. The purpose of this function is to facilitate a straightforward comparison between two solutions. Given parameter sets v_1 and v_2 from the domain Ω, where v_2 represents an improved configuration over v_1 concerning the desired objectives of the model, the cost function should satisfy the property (77).

$$C(v_2) < C(v_1) \tag{77}$$

The ultimate goal of the optimization process is to determine the optimal solution v_{opt} to the problem, which is mathematically expressed as in (78)

$$v_{opt} = \min_{v \in \Omega} C(v) \tag{78}$$

To find this minimum, various numerical algorithms can be utilized, with the choice depending on the specific problem and the number of variables involved. They can be sorted in two groups, the determinist algorithms one the one side and the stochastic on the other side. The deterministic algorithms such as Nelder-Mead, Newton, BFGS (Broyden-Fletcher-Goldfarb-Shanno) algorithms are locally convergent thus they tend not to find the global minimum. Stochastic algorithms such as PSO (Swarm optimization) or BO (Bayesian optimization) use a random component when choosing a point so that it has more chances to find the global minimum. A comparison of both types of algorithms was made by M. Wetter in [24] lead to the chose made in the future parts.

4.1.2 Chosen objective function

In the case of the rotor optimization, since it will be 3D printed with materials that have similar mechanical properties like shown in the table in Appendix B, it can be assumed that any changes in the rotor's shape does not significantly alter the mechanical stresses, and the rotor will remain in the elastic domain. Consequently, the mechanical stresses are not considered in the cost function.
The parameters being targeted for optimization are the maximum torque produced by the motor and the torque ripple (the amount of torque variation). Theses parameters have been chosen as they are the important when designing a motor. To combine these two objectives (maximum torque and minimum ripple), into a single scalar value for the optimization, a scaling factor β is introduced and defined as shown in (79) with T the torque θ, the load angle and R_{ipple} the amount of torque variation over time.

$$C = \max_{\theta}(T(\theta)) - \beta R_{ipple} \tag{79}$$

In this study, the scaling factor was set to 2, as it yielded the best results.
To determine the maximum torque, an initial simulation is conducted with a stationary magnetic field while rotating the rotor, as depicted in Figure 30. This allows us to obtain the torque characteristics of the motor. Subsequently, a sine wave function is fitted to this curve, representing the behavior of an ideal motor without saturation or ripple. The maximum value of this sine wave is then taken as the maximum torque. This approach helps mitigate the influence of small torque variations on the average torque value.

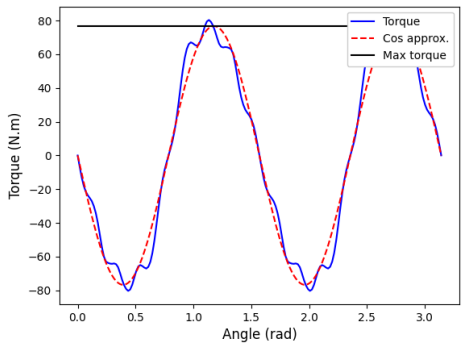

Figure 30: Simulation of the torque with a stationary magnetic field and rotating rotor

To compute the torque ripple, two methods are employed. The first method involves obtaining the maximum and minimum torque values over one-quarter turn in a time simulation where the magnetic filed rotates at the same speed as the rotor, as shown in Figure 31 and defined in equation (80). Since the torque exhibits periodic behavior for every quarter turn, the study can be limited to this duration.

$$R_{ipple} = \max_{t}(T(t)) - \min_{t}(T(t)) \tag{80}$$

This method is efficient in acquiring the torque ripple but may not always be feasible if the software lacks access to minimum and maximum tools (like COMSOL for optimization study [25]). Thus an other method needs to be used to calculate the minimum and maximum using continuous functions.

For this a simple way is to dived in 2 the torque, the part that is higher than the average and the part that is lower as can be done using these 2 math functions.

$$\begin{aligned} R^{+}_{ipple} &= \frac{(T(t)-\overline{T})+|(T(t)-\overline{T})|}{2} \\ R^{-}_{ipple} &= \frac{(T(t)-\overline{T})-|(T(t)-\overline{T})|}{2} \end{aligned} \tag{81}$$

Then an approximation of the maximum number in a list is given by the approximation of $||.||_{\infty}$ by using the convergence of the p-norm toward $||.||_{\infty}$ when p is high, the approximation of the ripple is

$$R^{\infty}_{ipple} = \left(\sum \left(R^{+}_{ipple}\right)^{p}\right)^{\frac{1}{p}} + \left(\sum \left(R^{-}_{ipple}\right)^{p}\right)^{\frac{1}{p}} \tag{82}$$

With a value of $p = 100$ the results are to 0.01 N.m from the real value calculated with the min max function. This method might not work for every problem as the value of the sum can get quite high and be higher than the maximum number allowed by the software.

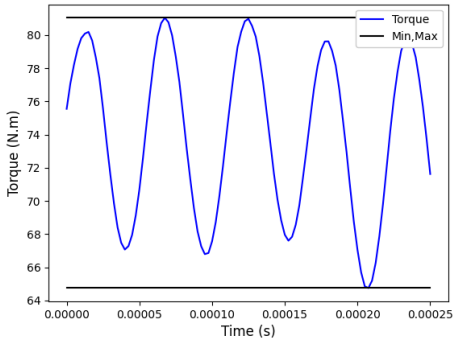

Figure 31: Simulated torque over time with min-max

For the next parts the torque ripple is calculated and expressed using the following formulation

$$T_{ripple} = \frac{\max(T) - \min(T)}{\overline{T}} \tag{83}$$

In the following parts two usual method of optimization are used together to get the best result possible. The first part is be dedicated to parametric optimization where global convergency is possible, the second part is about parametric optimization which converges locally. By combining these two steps near global convergency is feasible.

4.2 Parametric optimization

4.2.1 Set of parameters for the optimization

The concept behind parametric optimization is to use a fixed set of variables that represent material or geometrical properties in our model. This set of parameters is then optimized to find the most suitable values. Parametric optimization offers several advantages over other optimization methods. It often requires a smaller set of parameters, leading to faster convergence. Additionally, the final shape can be controlled for ease of manufacturing for example, as the basic geometry is defined by the user.
In our case, it was chosen to utilize Bézier curves to define the geometry. Despite their simplicity, Bézier curves allow us to represent complex shapes with just a few parameters, as shown in equation (84) and Figure 32.

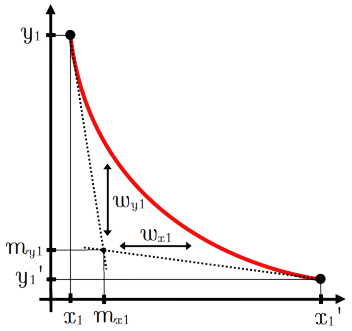

Figure 32: Example of a quadratic Bézier curve

$$x(\tau) = \frac{x_1(1-\tau)^2 + w_{x1}m_{x1}(1-\tau)\tau + x_1'\tau^2}{(1-\tau)^2 + w_{x1}(1-\tau)\tau + \tau^2} \qquad \tau \in [0,1] \tag{84}$$
$$y(\tau) = \frac{y_1(1-\tau)^2 + w_{y1}m_{y1}(1-\tau)\tau + y_1'\tau^2}{(1-\tau)^2 + w_{y1}(1-\tau)\tau + \tau^2} \qquad \tau \in [0,1]$$

To simplify the equations above, it was chosen to make the curve symmetric and place points (x_1, y_1) and (x_1', y_1') on a circle with the diameter of the rotor. This results in each Bézier curve having only three parameters: the positions of x_1 and m_1 on the x axis, and the weight w_1. With these new conditions, equation (85) describes the curves.

$$x(\tau) = \frac{x_1(1-\tau)^2 + w_1m_1(1-\tau)\tau + \tau^2\sqrt{r_{rotor}^2 - x_1^2}}{(1-\tau)^2 + w_1(1-\tau)\tau + \tau^2} \qquad \tau \in [0,1] \tag{85}$$
$$y(\tau) = \frac{(1-\tau)^2\sqrt{r_{rotor}^2 - x_1^2} + w_1m_1(1-\tau)\tau + x_1\tau^2}{(1-\tau)^2 + w_1(1-\tau)\tau + \tau^2} \qquad \tau \in [0,1]$$

By adding two curves, a new domain (a rib) can be defined with a different material. An additional parameter n specifies the number of rib, ranging from 1 to n_{rib}. However, this parameter does not change the total number of parameters. If fewer than n_{rib} rib are wanted, the unused rib parameters do not have an effect. The vector (86) of size $2n_{rib} \times 3 + 1$ forms the basis for the optimization.

$$v = [x_1, ..., x_{2n_{rib}}, m_1, ..., m_{2n_{rib}}, w_1, ..., w_{2n_{rib}}, n] \tag{86}$$

This set of parameters enables the representation of various shapes, as shown in Figure 33.

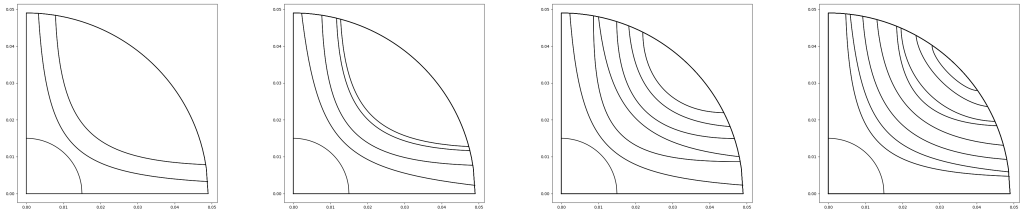

Figure 33: Examples of rotor shapes

One remaining issue with this set of parameters is that if the bonds are not properly defined, the geometry cannot be modeled accurately. Therefore, it is crucial to establish a set of bonds for the parameters.
First of address this concern, the coordinate system for the x_i and m_i parameters is changed to a cylindrical coordinate system. By doing so, the spacing between two points remains consistent regardless of their location on the circle. The equation (87) is used to compute the Bézier curves since their parameters are in the cartesian coordinate system.

$$x_{\text{cartesian}} = \sin\left(\frac{x_{\text{cylindrical}}}{r_{\text{rotor}}}\right) r_{\text{rotor}} \tag{87}$$

Then the x_i parameters are restricted to values between 0 and $\frac{\pi}{4}R_{\text{rotor}}$, which corresponds to the arc length for a 45° rotation. Similarly, the m_i points are confined between 0 and $\frac{\pi}{4}R_{\text{rotor}}$, ensuring that if $x_i = m_i$, the points (x_i, m_i, y_i) form a square triangle. Lastly, the w_i points are allowed to vary between 0 and ∞.

However, this parameter set presents some issues. The curves may intersect with each other, leading to problems in the model definition, as depicted in Figure 34.a . Additionally, when two curves are too close to each other, the mesh cannot be created, making the part challenging to manufacture, as shown in Figure 34.b . Furthermore, exchanging two curves results in the same solution introducing more potential local minimums in the cost function and complicating the search for the minimum as shown in Figure 34.c .

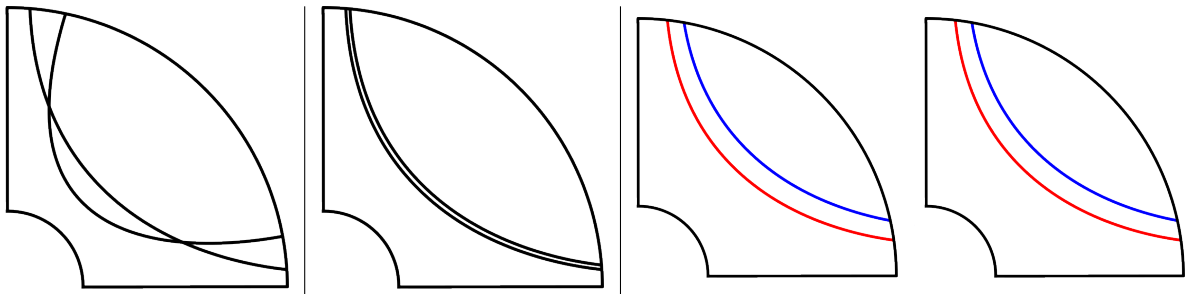

(a) overlapping (b) too close (c) double solution

Figure 34: Problems a, b and c

To resolve these problems, a solution is to sort all the parameters, add spacing between them, and reduce the bonds, as specified in equation (88):

$$\begin{array}{c} Sx_{ini} < x_1 < x_2 - Sx_{mid} < x_2 < ... < x_{2n_{rib}} - Sx_{mid} < x_{2n_{rib}} < r_{rotor}\frac{\pi}{4} - Sx_{end} \\ Sm_{ini} < m_1 < m_2 - Sm_{mid} < m_2 < ... < m_{2n_{rib}} - Sm_{mid} < m_{2n_{rib}} < \frac{r_{rotor}}{\sqrt{2}} - Sm_{end} \\ Sw_{ini} > w_1 > w_1 - Sw_{mid} > w_2 > ... > w_{2n_{rib}-1} - Sw_{mid} > w_{2n_{rib}} > Sw_{end} \end{array} \tag{88}$$

Consequently, the optimization parameter domain $\Omega_{n_{rib}}$ is defined, considering these bonds and constraints as in (90) domain

$$\Omega_{n_{rib}} = \left\{ x_1, ..., x_{2n_{rib}}, m_1, ..., m_{2n_{rib}}, w_1, ..., w_{2n_{rib}}, n \;\middle|\; \right. \tag{89}$$

$$\left. \begin{array}{c} Sx_{ini} < x_1 < x_2 - Sx_{mid} < x_2 < ... < x_{2n_{rib}} < r_{rotor}\frac{\pi}{4} - Sx_{end} \\ Sm_{ini} < m_1 < m_2 - Sm_{mid} < m_2 < ... < m_{2n_{rib}} < \frac{r_{rotor}}{\sqrt{2}} - Sm_{end} \\ Sw_{ini} > w_1 > w_1 - Sw_{mid} > w_2 > ... > w_{2n_{rib}} > Sw_{end} \\ n \in [\![1, n_{rib}]\!] \end{array} \right\} \tag{90}$$

This domain definition ensures that the model is well-defined for each set of parameters. However, finding a point within this domain, if the initial point is chosen randomly, is unlikely (probability $\frac{1}{(2n_{rib})!}$ in an initial domain with the same bonds but not sorted). Thus, a method is required to transition from a simple domain, such as the unit ball of radius one, to the domain $\Omega_{n_{rib}}$.
A new domain, Ω_m^a, is introduced, defined as follows in (91). It represents the domain from which values are selected. Finding random values in this domain is really easy because it is a square domain with values Independent from each others.

$$\Omega_m^a = \{a_1, ..., a_m \in [0, 1]^m\} \tag{91}$$

To convert this domain to the unit ball with respect to the norm $||.||_\infty$, a simple bijective affine function, given by equation (92), is employed:

$$f_1 : \Omega_m^a \to [-1,1]^m \; v \to 2v - (1,...,1) \tag{92}$$

Additionally, it is known that every compact convex space, such as Ω_m^b ((93)) defined in (93), is homeomorphic to the unit ball of radius 1 with respect to the $||.||_\infty$ norm. Therefore, a bijection can be established between these two spaces using the gauge function, as described by the following function

$$\Omega_n^b = \{b_1, ..., b_m \in [0,1]^m \quad | \quad b_1 < ... < b_m\} \tag{93}$$

$$f_2 : [-1,1]^m \to \Omega_m^b \; x \to \frac{x||x||_\infty}{j(x)} + \left(\frac{1}{m+1}, ..., \frac{m}{m+1}\right) \tag{94}$$

With j the gauge function defined as

$$j(x) = \inf_\lambda \left\{\lambda > 0 \quad \middle| \quad \frac{x}{\lambda} \in \left(\Omega_m^b - \left(\frac{1}{m+1}, ..., \frac{m}{m+1}\right)\right)\right\} = (m+1)\max\left(0, -x_1, x_m, \max_{k \in [\![1, m-1]\!]}(x_k - x_{k+1})\right) \tag{95}$$

To visualize this function, random points in $[0,1]^2$ are plotted, and their values through this function are shown in Figure 35. The complete mathematical demonstration can be found in a lesson by R. Texier-Picard [26]

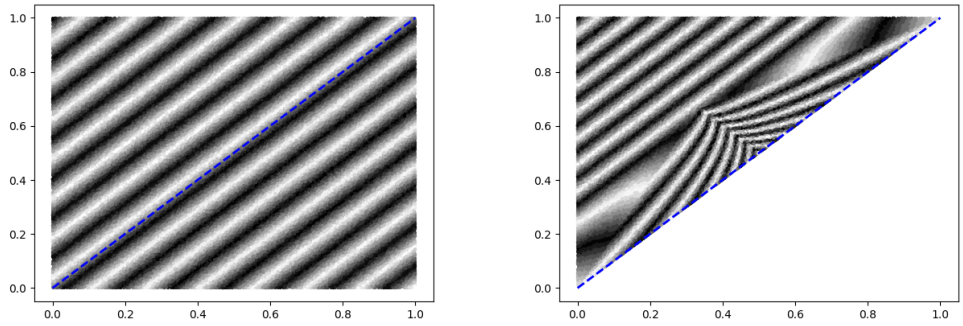

Figure 35: Input points and Image points

Once the elements are sorted and restricted to values between 0 and 1, they can be translated to the appropriate size for the rotor's shape. Thus, a third function is created, defined in (96):

$$f_3 : \begin{matrix} \Omega_{6n_{rib}+1}^b \to \Omega_{n_{rib}} \\ b_1, ..., b_{3n_{rib}+1} \to a, b, c, d \end{matrix} \tag{96}$$

where:

$$a = Sx_{ini} + \lambda_x b_1, Sx_{ini} + \lambda_x b_2 + Sx_{mid}, ..., Sx_{ini} + \lambda_x b_{2n_{rib}} + Sx_{mid}(2n_{rib} - 1)$$
$$b = Sm_{ini} + \lambda_m b_{2n_{rib}+1}, Sm_{ini} + \lambda_m b_{2n_{rib}+2} + Sm_{mid}, ..., Sm_{ini} + \lambda_m b_{4n_{rib}} + Sm_{mid}(2n_{rib} - 1)$$
$$c = Sw_{ini} + \lambda_w(1 - b_{4n_{rib}+1}) + Sw_{mid}(2n_{rib} - 1), Sw_{ini} + \lambda_w(1 - b_{4n_{rib}+2}) + Sw_{mid}(2n_{rib} - 2), ..., Sw_{ini} + \lambda_w(1 - b_{6n_{rib}})$$
$$d = \min\left((n_{rib} b_{3n_{rib}+1} \vdash 1) + 1, n_{rib}\right)$$

with:

$$\begin{aligned} \lambda_x = &\quad (Sx_{fin} - Sx_{ini} - (n_{rib} - 1)Sx_{mid}) \\ \lambda_m = &\quad (Sm_{fin} - Sm_{ini} - (n_{rib} - 1)Sm_{mid}) \\ \lambda_w = &\quad (Sw_{fin} - Sw_{ini} - (n_{rib} - 1)Sw_{mid}) \end{aligned}$$

Finally, the three functions can be combined, establishing a direct link between $\Omega^a_{6n_{\text{rib}}+1}$ and $\Omega_{n_{rib}}$, as illustrated in equation such that

$$\Omega_{n_{rib}} = f_3 \circ f_2 \circ f_1 \left(\Omega^a_{6n_{\text{rib}}+1}\right) \tag{97}$$

This function ensures that every possible input vector in $[0,1]^{6n_{\text{rib}}+1}$ results in a geometry that can be constructed, and is unique.

4.2.2 Computation of the cost function

Now that an algorithm capable of minimizing high-cost functions as been developed, the cost function needs to be computed. As an input, this function should takes the geometric parameters and output the torque curve as a function of the load angle θ and t. To achieve this, the software COMSOL is used. In COMSOL a Finite Element Model (FEM) is set up, in such a way that the geometry can be adjusted by the input parameters, as illustrated in Figure 36. This model is explained in more details in the Appendix A.

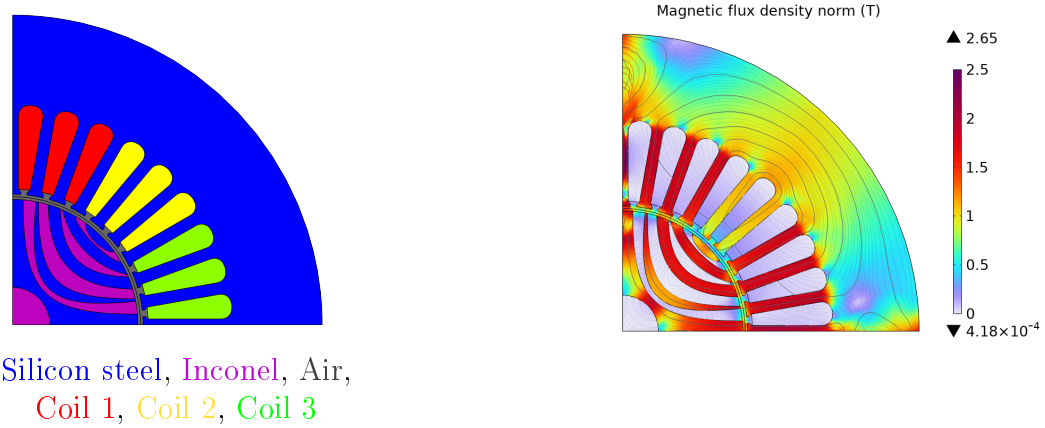

Figure 36: COMSOL model geometry and magnetic field result for one load angle

Next, two simulations are performed, one is a time simulation that provides the torque function over time, and the other is a sweep DC simulation with different load angles. Both simulations export a file that can be read by a Python script. To automate the simulations with different parameters, the MPh library [27] is used, which serves as a COMSOL Python bridge. Due to model constraints, changing the number of ribs directly in the model causes errors. Therefore, multiple files with different numbers of ribs are created then the file with the desired number of ribs is called. After each iteration, the model is removed from memory to prevent unnecessary memory usage.

As a reference solution for the optimization the torque and torque ripple were computed with a basic geometry (Figure 37) to serve as a reference for the optimized shape.

$$\begin{gathered}\text{Final cost} = 14.6 \\ \text{Max Torque} = 78.2 \quad \text{N.m} \\ \text{Torque ripple with min-max criteria} = 40.6\ \%\end{gathered} \tag{98}$$

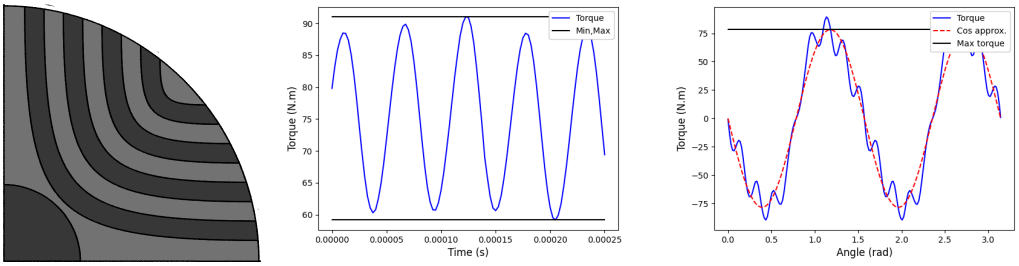

Figure 37: Reference shape, ripple and torque

4.2.3 Minimizing method

The minimization process involves numerically finding the set of input parameters that minimize the cost function. The choice of minimization algorithms depends on several factors, including the computing time of the cost function, the number of input variables, and the presence of local minima.
If the cost function's computing time is low, there are only a few variables and no local minima are present, standard gradient-based algorithms are suitable. However, in our case, the cost function's evaluation is time-consuming (around one minute) due to the 2D electromagnetic simulation launched at each iteration, the number of variables is high (25 for 4 rib), and they are many local minima, thus gradient based algorithms can not work in this case.
To address these challenges, a three step approach to solve this minimization problem is adopted and detailed in the following parts

4.2.3.1 Random exploration

The first phase involves a random exploration of the function. This serves two purposes, firstly, it allows the final solution not to be overly dependent on a good initial solution, which can be difficult to find, secondly, it helps identify potential starting points that may lead to local minima.

4.2.3.2 Bayesian minimization

The second step uses a Bayesian algorithm to approximate the global minimum. The Bayesian optimization works by creating uncertainty intervals based on Gaussian processes using the data obtained from the previous random exploration step, as explained by J. Mockus in [28], and depicted in Figure 38.a. The algorithm creates a new function called the utility function which is based on the mean of the Gaussian process and it's covariance, then the algorithm evaluates the cost function on the lowest point of the utility function function 38.b . This process is repeated until the desired number of iterations is reached, as depicted in Figure 38.c . For all of the results the covariance, or Kernel used was the Matern 2.5, the α parameter (incertitude in the values of the cost function) was set to 10^{-6} and the κ parameter (balance between exploration and convergency) to 2.576. Promising results were shown with $\alpha = 10^{-10}$ and $\kappa = 0.5$ but more experimentation is still needed fine tune theses parameters.

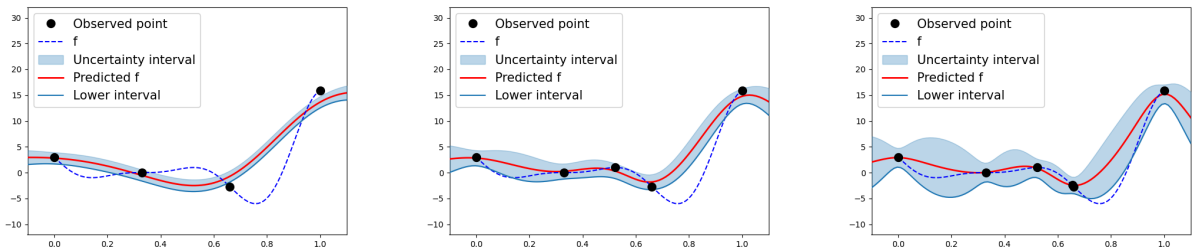

(a) Initial step (b) Second step (c) Final step

Figure 38: Bayesian optimization

The advantage of this algorithm is that it uses all known data at each step to find the next point. However, one issue remains: if multiple local minima have nearly the same cost as the global minimum (which is the case with our rotor), the algorithm will oscillate between these multiple points, resulting in slow convergence. Furthermore if the number of evaluation is very high the computing time of the new point can slow down the process (160 seconds to find a new point after 5000 iterations). Therefore, a final step is needed to address this.

4.2.3.3 Nelder and mead

The final step involves using a Nelder-Mead algorithm on the best value found by the Bayesian algorithm. While the solution found by Bayesian optimization may not be the global minimum, it is a local minimum that closely approximates or matches the global minimum in terms of cost function value. Consequently, this point can be adopted as the initial starting point for the Nelder-Mead algorithm.
The Nelder and Mead algorithm, introduced by A. Nelder in [29] is a non stochastic algorithm, it uses a polytope of dimension one higher than the problem dimensions. It changes one point of this polytope, evaluates the function at this new point, and then computes which point should be changed and where, as shown in Figure 39. This algorithm converges faster for non-linear functions than gradient based algorithms and can easily be constrained by bonds, but as it is non stochastic it only ensures convergence toward a local minimum.

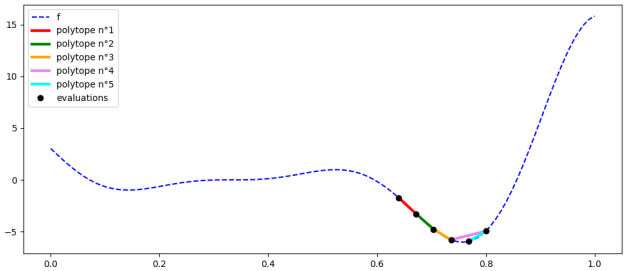

Figure 39: First five steps of Nelder Mead optimization

4.2.4 Results of parametric optimization

To use this optimization process effectively, the first step is to find a suitable scaling factor β for the problem defined in (79). This is accomplished by running the program multiple times with different values of β (with arround 10 times the number of variables as the maximum number of iterations) and observing the effects on torque and torque ripple. A balanced value of $\beta = 2$ is found in our case, where an increase in torque also results in a decrease in torque ripple.

A simulation is then launched with a high number of iterations around 20 times the number of variables for the number of random initial points. The Bayesian optimization part benefits from a higher number of iterations, as initial convergence is fast, but further improvements are achieved after a few thousand iterations. Approximately 200 times the number of parameters is a suitable number of iterations for this problem. Finally, the Nelder Mead algorithm requires very few iterations to converge to a local minimum, typically between 10 and 20 times the number of variables.
The convergence plot in Figure 40 demonstrates that the overall number of iterations could be reduced while still yielding good results. However, maintaining a high number of iterations helps reduce the impact of luck during the initial random phase.
Once the algorithm completes all iterations, the final shape can be obtained, as shown in Figure 41. The final torque and torque ripple can then be computed giving the following results:

$$\begin{gathered}\text{Final cost} = 79.4 \\ \text{Max Torque} = 86.0 \quad \text{N.m} \\ \text{Torque ripple with min-max criteria} = 3.9\ \%\end{gathered} \tag{99}$$

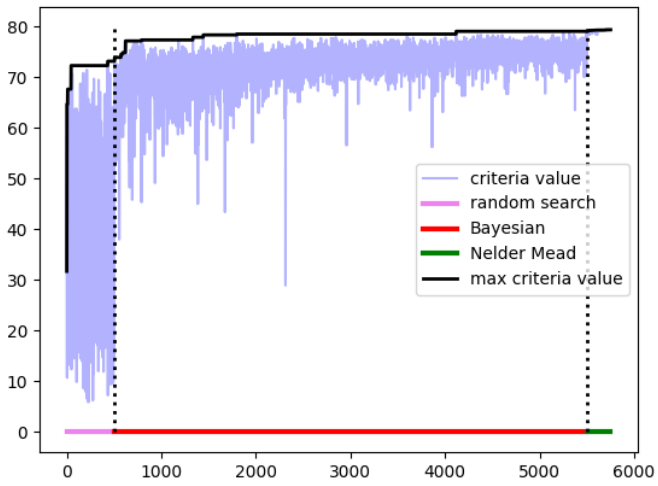

Figure 40: Evolution of the cost function of iterations

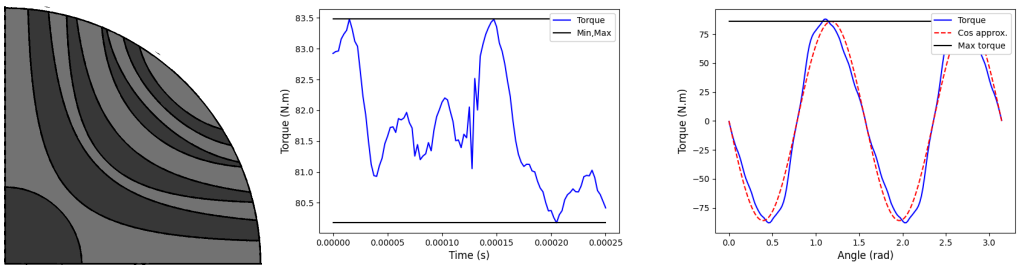

Figure 41: shape, ripple and torque after 500+5000+250 iterations

4.3 Topology optimization

Topology optimization is another type of optimization with the same overall objective as parametric optimization, finding the best geometry and material for a given criteria. However, in

topology optimization, there are no input parameters specified by the user, leading to more diverse shapes as shown by M. Beckers [30]. As a consequence, there is no possibility for random exploration at the beginning because of the amount of design variables (up to 30000 in [30]) , so topology optimization procedures must start with a good initial geometry and material parameters for the shape.

4.3.1 Construction of the optimal shape

To allow the optimization algorithm to explore different shapes, a mathematical function representing the shape needs to be created. In this study, boundary topology optimization is used, where the algorithm changes only the shape of the boundary without modifying the material parameters, as could be done in usual topology optimization.

As explained by E. Shakour in [31] a density function with values between -1 and 1 is defined for the complete part domain using B-spline surfaces to represent the shape. The shape is then intersected with a plane where the density value is 0 everywhere, resulting in the boundary that defines the part's shape. The initial parameters for the B-spline are chosen to match the user-defined initial shape as shown in the Figure 42.

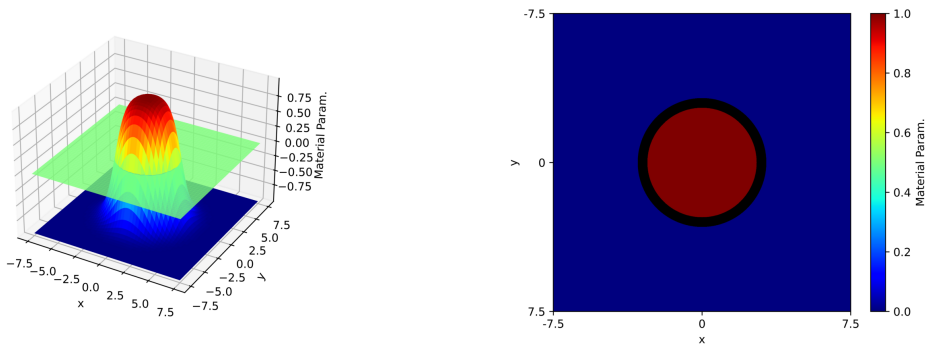

Figure 42: Initial shape definition

Once the input parameters are defined, the process follows similar steps to parametric optimization. An algorithm attempts to find the set of parameters that minimizes the cost function. However, this cost function is more challenging to minimize due to the higher number of parameters (around 250 for the rotor). For such cases, Bayesian minimization may not work effectively. A non-stochastic gradient-based method called SNOPT (Sparse Nonlinear OPTimizer) is utilized to find a local minimum, as described extensively by E. Philip in [32]. This method utilizes a quadratic polynomial approximation of the cost function to find each new iteration point. It is essential to have a good initial guess, as the algorithm may converge toward a local minimum rather than a global minimum. Once the new set of parameters is obtained, the density function is intersected with a plane to generate a new geometry as in the Figure 43, and the process iterates to find the best possible solution.

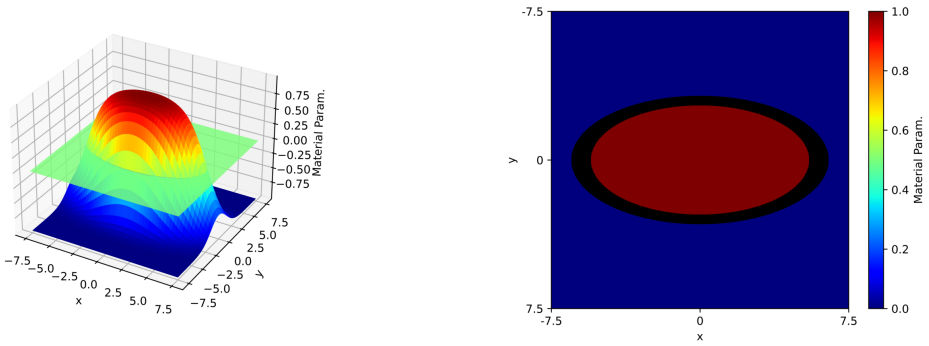

Figure 43: Next step in the optimization

4.3.2 Topology optimization results

Topology optimization was directly done in COMSOL, as the software already integrates the necessary tools. Only the ribs boundary,were allowed to be modified and moved by a maximum of 1.5mm to avoid overlapping, similarly to parametric optimization. However, the cost function used here differed since COMSOL does not support minimum and maximum evaluations in the cost function. Instead, the integral of the torque ripple was used as the cost function in a time-dependent study. The maximum torque was computed before launching the program, and the angle of maximum torque was inputted in the time-dependent study. It is assumed that this angle does not change significantly during the optimization; otherwise, a new optimization must be started with the updated value.
The initial results obtained using this topology optimization method were based on an initial shape defined by equally spaced Bézier curves with the same parameters as shown in 37. The results are presented in Figure 44 and in (100).

$$\begin{aligned} \text{Final cost} &= 16.0 \\ \text{Max Torque} &= 81.2 \quad \text{N.m} \\ \text{Torque ripple with min-max criteria} &= 40\% \end{aligned} \tag{100}$$

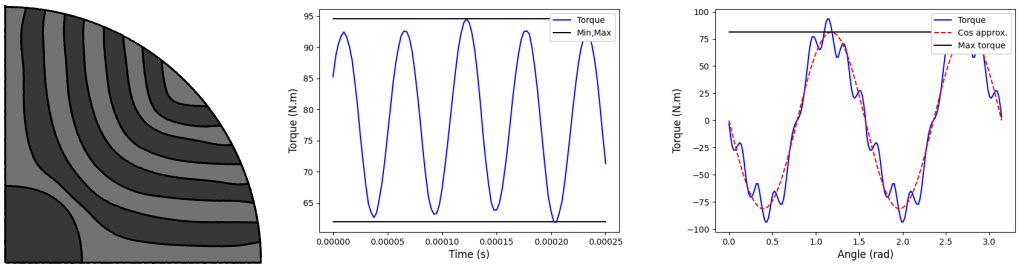

Figure 44: Shape, ripple, and torque after 100 iterations of the SNOPT solver

4.4 Optimization results

For the final results, a combination of the two different optimization procedures was used. Since topology optimization requires a good initial solution, the decision was made to input the results of the parametric optimization as the inital step of the topology optimization. This approach allows the topology optimization to start with an already almost optimal shape, leading to better convergence toward a minimum compared to topology optimization of a basic shape.

The final results are shown in equation (101) and Figure 45. The torque ripple value used for the optimization was the R^{∞}_{ipple}

$$\begin{gathered} \text{Final cost} = 79.7 \\ \text{Max Torque} = 87.4 \quad \text{N.m} \\ \text{Torque ripple with min-max criteria} = 4.4\ \% \end{gathered} \tag{101}$$

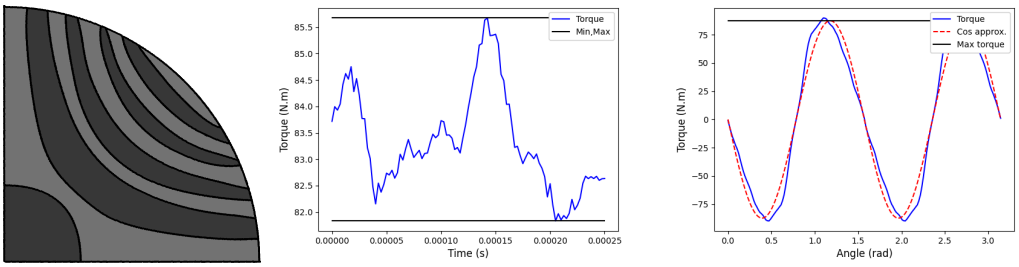

Figure 45: Shape, ripple, and torque after 100 iterations of the SNOPT solver

Finally, all the results are summarized in the following table:

Method Used	Final cost	Maximum torque	Ripple	Max efficiency	Max power factor
None	14.6	78.2 N.m	40.6 %	98.0 %	0.47
Topology	16.0	81.2 N.m	40.0 %	98.4 %	0.50
Parametric	79.4	86.0 N.m	3.9 %	98.6 %	0.51
Topology and Parametric	79.7	87.4 N.m	4.4 %	98.6 %	0.53

It should be noted that all of these results have been computed using the same model (for torque, torque ripple, maximum power factor and maximum efficiency) and using the same cost function for the final cost.

The combined approach using both topology and parametric optimizations yields a much better result than using either method alone. This result was suggested by T.H. Lee in [33]. However, their approach lacked degrees of freedom in parametric optimization and a more powerful minimizing process, leading to suboptimal solutions even after topology optimization. With the presented combined approach, every possible solution can be explored, ensuring that the final solution is optimal. Moreover, the objective function considers torque ripple and maximum torque, simplifying the design process as additional methods to reduce the ripple are not needed. In addition the process can be easily controlled to match manufacturing tolerances.

5 Conclusion

During this work, solutions were proposed to solve the main issues in high-speed synchronous motors regarding the mechanical strength of the rotor and its performance. By using a novel approach to build the motor's rotor from two different materials, one magnetic and the other non-magnetic, and changing the shape of the shaft, a rotor was obtained that enables high-speed rotation while still being easy to manufacture. Furthermore, this new building approach enables new optimization possibilities that were not previously possible due to mechanical failure of the rotor.

This type of approach shows promise, but further research needs to be conducted. The nature of the bond between Inconel and silicon steel has not been demonstrated experimentally. Therefore, testing needs to be done to ensure that the building process corresponds to the manufacturing data and that the processes occurring during the HIP cycle align with the descriptions provided earlier. Experimentation would also help in obtaining experimental data for the diffusion parameters and the material parameters.

The idea of changing the shape of the shaft has helped us reduce the amount of stress in the rotor. However, another unexplored option would be to print the shaft directly into the rotor, benefiting from a strong bond between the rotor and the shaft.

Finally, the optimization process could be significantly improved. The topology optimization algorithm used is the one provided directly by COMSOL, which is neither fast nor convergent toward the best solution. The parametric optimization process could also be enhanced. Increasing the maximum number of ribs might reveal a clearer selection in the number of ribs, as opposed to the best solution being the maximum number of ribs. Additionally, the Bayesian optimization process could be fine-tuned further by adjusting the kernel and the values of the α and κ coefficients.

Appendix A : Electromagnetic model of a *SynRm* motor

This appendix details the electromagnetic model made in COMSOL that was used to calculate the eddy current losses, the torque of the motor over time and for different load angles, the power factor and the efficiency. This procedure of modeling in not unique and similar results have already been shown by A. Bentounsi in [34] for example.

Initial setup of the model

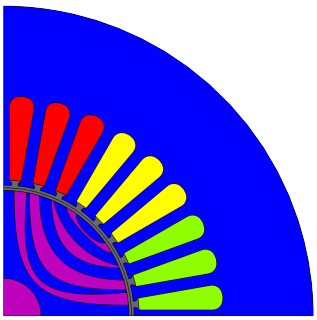

Silicon steel, Inconel, Air,
Coil 1, Coil 2, Coil 3

Figure 46: Motor domains

As shown in the Figure 46, the simulation is based on a 2D model which is only a quarter of the full rotor. This is possible because of the periodic conditions and the sector symmetry. As a result the model in less complicated but still gives the same results. Magnetic insulation is used on the outer perimeter as a boundary condition.
The blue part is silicon steel, it is considered as a non linear magnetic material, that way the effect of the magnetic saturation can be seen. The values for the B(H) curve is obtained using experimental data and then interpolated.

The purple part is considered as a linear magnetic material with a relative permeability of one as it is a non magnetic material.

The blue, purple and half of the grey parts form the rotating domain of the motor, this domain is rotated by an angle θ_m

The red yellow and green part are the coils used, in this area the input current is defined as follows with θ_e the electrical angle and I_0 the maximum current (231A in our case)

$$\begin{aligned} I_{coil1} &= I_0 \cos(\theta_e) \\ I_{coil2} &= -I_0 \cos(\theta_e - \tfrac{2\pi}{3}) \\ I_{coil3} &= I_0 \cos(\theta_e - \tfrac{4\pi}{3}) \end{aligned} \tag{102}$$

From all of these parameters COMSOL solves the Maxwell equations using the finite element method using $\mathbf{A}$ the magnetic vector.

Types of simulations

First the load angle θ is defined as

$$\theta = \theta_m - \frac{2}{N_p}\theta_e \tag{103}$$

With N_p the number of poles of the motor (In our case 4)
Then θ_e is fixed to one value and the value of θ is changed. That way the torque can be computed for different load angles with a static magnetic filed. This type of study is called a **sweep DC** study as the current is in the coils is not changing.

An other type of simulation is to take the load angle as stationary and rotate the electrical field and the angle of the rotor at the same time. With this simulation the torque of the motor while it is turning is computed. This is called a **time simulation** and the different angles are defined as follow with ω the rotating speed of the motor in rad.s^{-1} and t the time in s.

$$\theta_e = \frac{N_p}{2}\omega t \tag{104}$$

$$\theta_m = \omega t + \theta \tag{105}$$

Calculation of the torque

In all of the simulations the torque was calculated using the Arkkio's formulation as described by N.Sadowski in [35]. The torque can thus be described as

$$T = \frac{l}{\mu_0(r_{out} - r_{in})} \int_S B_r B_\theta r dS \tag{106}$$

With B_r and B_θ the radial and circumferential components of the magnetic filed on a circle of radius r witch is between the rotor and stator. l is the length of the rotor.

Calculation of the eddy currents

As as result of solving the Maxwell equations it is easy to get the electric filed **E** and the current field **J**. Thus the time average of the power losses can be calculated. as follow

$$P_{los} = \frac{1}{t} \int_v \int_0^t \mathbf{J} \cdot \mathbf{E} dt dv \tag{107}$$

This is computed in 2D, thus the results are not the same as in 3D since some effects are neglected in 2D, but from one simulation to an other the results are comparable.

Calculation of the efficiency

To calculate the efficiency first the losses are calculated for each part of the motor (P_{rot},P_{stat},P_{coil})
Then the output power is calculated by taking the average of the torque $\overline{T}$ multiplied by the rotation speed.
Then the efficiency $\eta_{\%}$ can be calculated like so

$$\eta_{\%} = \frac{\overline{T}\omega}{\overline{T}\omega + P_{rot} + P_{stat} + P_{coil}} \tag{108}$$

Calculation of the power factor

The first step is to find the current and flux in in the dq coordinate with the axis d and q being the the axis of highest inductance and lowest inductance respectively. For this projection the Clarke matrix is used as follow

$$\begin{pmatrix} I_d \\ I_q \end{pmatrix} = \frac{2}{3} \begin{pmatrix} \cos(\theta) & \cos(\theta) - \frac{2\pi}{3} & \cos(\theta) - \frac{4\pi}{3} \\ \sin(\theta) & \sin(\theta) - \frac{2\pi}{3} & \sin(\theta) - \frac{4\pi}{3} \end{pmatrix} \begin{pmatrix} I_{coil1} \\ I_{coil2} \\ I_{coil3} \end{pmatrix} \tag{109}$$
$$\begin{pmatrix} \phi_d \\ \phi_q \end{pmatrix} = \frac{2}{3} \begin{pmatrix} \cos(\theta) & \cos(\theta) - \frac{2\pi}{3} & \cos(\theta) - \frac{4\pi}{3} \\ \sin(\theta) & \sin(\theta) - \frac{2\pi}{3} & \sin(\theta) - \frac{4\pi}{3} \end{pmatrix} \begin{pmatrix} \phi_{coil1} \\ \phi_{coil2} \\ \phi_{coil3} \end{pmatrix}$$

Then the inductances L_i^d and L_i^q in those 2 orientations can be calculated as follow when the current is not 0.

$$L_i^q = \frac{\phi_q}{I_q} \tag{110}$$
$$L_i^d = \frac{\phi_d}{I_d}$$

Then the voltages V_d and V_q can be calculated as follow with R_s the stator winding resistance (O.E. Ozcciflikcci in [36])

$$V_d = R_s I_d + L_d \frac{dI_d}{dt} - L_i^q \omega_e I_q \tag{111}$$
$$V_q = R_s I_q + L_q \frac{dI_q}{dt} - L_i^d \omega_e I_d \tag{112}$$

Assuming that R_s is low and that I_d and I_q are independent of time (stationary simulation) the previous equations can be simplified as follows

$$V_q = -\omega_e L_i^q I_q \tag{113}$$
$$V_d = \omega_e L_i^d I_d$$

Finally the power factor $\cos\phi$ can be calculated as so

$$cos\phi = \cos\left(\text{atan2}\left(I_q, I_d\right) - \text{atan2}\left(V_q, V_d\right)\right) \tag{114}$$

Appendix B : Material properties

Material	**Silicon steel 3%**	**Inconel 625**
Volumique mass ($kg.m^{-3}$)	7310	8440
Young Modulus (GPa)	200	207
Yield stress (MPa)	231	414
Poisson ratio (s.u.)	0.32	0.28
Thermal expansion coefficient (K^{-1})	1.5×10^{-5}	1.3×10^{-5}
Thermal conductivity ($W.m^{-1}.K^{-1}$)	19	5.8
Electrical conductivity ($S.m^{-1}$)	2.17×10^{6}	8.00×10^{5}
Initial magnetic suseptibility (s.u.)	4000	1

Appendix C : Geometry of the rotor and stator

Geometry parameter	**Value**
Rotor radius (mm)	49
Shaft radius (mm)	15
Air gap length (mm)	2
Stator internal radius (mm)	51
Stator external radius (mm)	121
Number of poles	4
Number of stator slot	36
Slot height (mm)	35
Slot opening width (mm)	3
Rotor and stator length (mm)	135

References

[1] Andrea Credo, Giuseppe Fabri, Marco Villani, and Mircea Popescu. High speed synchronous reluctance motors for electric vehicles: A focus on rotor mechanical design. In *2019 IEEE International Electric Machines and Drives Conference (IEMDC)*, pages 165–171. IEEE, 2019.

[2] Christof Zwyssig. *An ultra-high-speed electrical drive system*. PhD thesis, Eidgenössische Technische Hochschule Zürich, 2008.

[3] Giampaolo Buticchi, David Gerada, Luigi Alberti, Michael Galea, Pat Wheeler, Serhiy Bozhko, Sergei Peresada, He Zhang, Chengming Zhang, and Chris Gerada. Challenges of the optimization of a high-speed induction machine for naval applications. *Energies*, 12(12):2431, 2019.

[4] Zhiyan Zhang, Hongzhong Ma, Cunxiang Yang, and Duanlei Yuan. Study on permanent magnet synchronous demagnetization fault performance. *Sensors and Transducers*, 173(6):82, 2014.

[5] Thomas Lipo. Synchronous reluctance machines-a viable alternative for ac drives? *Electric Machines and Power Systems - ELEC MACH POWER SYST*, 19:659–671, 11 1991.

[6] Zlatko Kolondzowski et al. Thermal and mechanical analyses of high-speed permanent-magnet electrical machines. 2010.

[7] Gianmario Pellegrino, Eric Armando, Paolo Guglielmi, and Alfredo Vagati. A 250kw transverse-laminated synchronous reluctance motor. In *2009 13th European Conference on Power Electronics and Applications*, pages 1–10. IEEE, 2009.

[8] Anouar Belahcen, Maksim A Sitnikov, and Sergey A Galunin. Optimization of a high-speed synchronous reluctance machine's rotor topology. In *2021 International Conference on Electrotechnical Complexes and Systems (ICOECS)*, pages 279–284. IEEE, 2021.

[9] Kevin Grace, Steven Galioto, Karthik Bodla, and Ayman M El-Refaie. Design and testing of a carbon-fiber-wrapped synchronous reluctance traction motor. *IEEE Transactions on Industry Applications*, 54(5):4207–4217, 2018.

[10] Valerii Abramenko, Ilya Petrov, Janne Nerg, and Juha Pyrhönen. Synchronous reluctance motors with an axially laminated anisotropic rotor as an alternative in high-speed applications. *IEEE Access*, 8:29149–29158, 2020.

[11] Grid Logic web site, howpublished = https://www.grid-logic.com.

[12] Valerii Abramenko. Synchronous reluctance motor with an axially laminated anisotropic rotor in high-speed applications. 2023.

[13] HV Atkinson and S Davies. Fundamental aspects of hot isostatic pressing: an overview. *Metallurgical and materials transactions A*, 31:2981–3000, 2000.

[14] Chao Cai, Bo Song, Qingsong Wei, Wu Yan, Pengju Xue, and Yusheng Shi. Effect of tooling material on the internal surface quality of ti6al4v parts fabricated by hot isostatic pressing. *Metallurgical and Materials Transactions A*, 48:34–38, 2017.

[15] JK Tien, JC Borofka, BC Hendrix, T Caulfield, and SH Reichman. Densification of oxide superconductors by hot isostatic pressing. *Metallurgical Transactions A*, 19:1841–1847, 1988.

[16] The Engineering ToolBox, howpublished = https://www.engineeringtoolbox.com/.

[17] Koji Arioka, Yoshiaki Iijima, and Tomoki Miyamoto. Rapid nickel diffusion in cold-worked carbon steel at 320–450 c. *Philosophical Magazine*, 95(32):3577–3589, 2015.

[18] John Crank. *The mathematics of diffusion*. Oxford university press, 1979.

[19] Svante Arrhenius. Uber die dissociationswarme und den einfluss der temperatur auf den dissociationsgrad der elektrolyte. *Zeitschrift fur physikalische Chemie*, 4(1):96–116, 1889.

[20] Solving the diffusion equation, howpublished = https://www.uni-muenster.de.

[21] Martin Lévesque. Mec6418 - notes de cours, homogénéisation analytique. pages 27–28, 2011.

[22] Daniel Iruikwu et al. In plane numerical analysis of mechanical stress in a synchronous reluctance machine. Master's thesis, 2013.

[23] Hideki Ohguchi, Takehisa Hirayama, Shion Takigawa, and Satoshi Imamori. Slot number dependence of in-plane eddy-current loss in electrical steel sheets of 6-pole permanent-magnet synchronous machines. In *2021 24th International Conference on Electrical Machines and Systems (ICEMS)*, pages 360–364. IEEE, 2021.

[24] Michael Wetter and Jonathan Wright. A comparison of deterministic and probabilistic optimization algorithms for nonsmooth simulation-based optimization. *Building and environment*, 39(8):989–999, 2004.

[25] Opitimization module, user's guide, author=COMSOL, howpublished = https://doc.comsol.com/5.4/doc/com.comsol.help.opt/OptimizationModuleUsersGuide.pdf.

[26] Notes de cours - Préparation à l'agréegation Convexité et applications, author=Rozenn Texier-Picard, howpublished = https://agreg-maths.univ-rennes1.fr/journal/2019/convexite.pdf.

[27] Mph web site, howpublished = https://mph.readthedocs.io/.

[28] Jonas Mockus and Jonas Mockus. *The Bayesian approach to local optimization*. Springer, 1989.

[29] John A Nelder and Roger Mead. A simplex method for function minimization. *The computer journal*, 7(4):308–313, 1965.

[30] Muriel Beckers. Topology optimization using a dual method with discrete variables. *Structural optimization*, 17:14–24, 1999.

[31] Emad Shakour and Oded Amir. Topology optimization with precise evolving boundaries based on iga and untrimming techniques. *Computer Methods in Applied Mechanics and Engineering*, 374:113564, 2021.

[32] E Philip, Walter Murray, and Michael A Saunders. User's guide for snopt version 7: Software for large-scale nonlinear programming. *SNOPT% 20Manual. pdf*, 2015.

[33] Tae-Hee Lee, Dong-Kuk Lim, Ki-Young Moon, and Kyung-Won Jeon. Topology optimization combined with a parametric algorithm for industrial synchronous reluctance motor design. *Processes*, 10(4):746, 2022.

[34] Khelifa Hocine, Bentounsi Ammar, and Rebahi Fares. Fe modeling and simulation of a synchronous reluctance motor based on comsol multiphysics. In *2019 19th International Symposium on Electromagnetic Fields in Mechatronics, Electrical and Electronic Engineering (ISEF)*, pages 1–2. IEEE, 2019.

[35] Nelson Sadowski, Yvan Lefèvre, Michel Lajoie-Mazenc, and Jérôme Cros. Finite element torque calculation in electrical machines while considering the movement. *IEEE transactions on magnetics*, 28(2):1410–1413, 1992.

[36] Ozcciflikcci Osman Emre and Mikail. Analysis of the saliency ratio effect on the output torque and the system efficiency in ipm drives. *Sakarya University Journal of Science*, 25(6):1417–1426, 2021.